

UNCLASSIFIED

AD NUMBER

AD436251

LIMITATION CHANGES

TO:

Approved for public release; distribution is unlimited.

FROM:

Distribution authorized to U.S. Gov't. agencies and their contractors;  
Administrative/Operational Use; 31 MAR 1964.  
Other requests shall be referred to Army Ballistic Research Laboratory, Aberdeen, Proving Ground, MD 21005.

AUTHORITY

AMC ltr, 31 Jan 1967

THIS PAGE IS UNCLASSIFIED

**UNCLASSIFIED**

**AD 436251**

**DEFENSE DOCUMENTATION CENTER**

**FOR**

**SCIENTIFIC AND TECHNICAL INFORMATION**

**CAMERON STATION, ALEXANDRIA, VIRGINIA**



**UNCLASSIFIED**

NOTICE: When government or other drawings, specifications or other data are used for any purpose other than in connection with a definitely related government procurement operation, the U. S. Government thereby incurs no responsibility, nor any obligation whatsoever; and the fact that the Government may have formulated, furnished, or in any way supplied the said drawings, specifications, or other data is not to be regarded by implication or otherwise as in any manner licensing the holder or any other person or corporation, or conveying any rights or permission to manufacture, use or sell any patented invention that may in any way be related thereto.

436251

**GENERAL ATOMIC**

DIVISION OF **GENERAL DYNAMICS**

436251

GA-5119

SUMMARY REPORT  
ON THE THEORY OF HYPERVELOCITY IMPACT

Advanced Research Projects Agency  
ARPA Order No. 71-62

Monitored by  
Ballistic Research Laboratories  
Army Contract DA-04-495-AMC-116(X)

March 31, 1964

NO. OTS

**GENERAL ATOMIC**  
DIVISION OF  
**GENERAL DYNAMICS**

JOHN JAY HOPKINS LABORATORY FOR PURE AND APPLIED SCIENCE

P.O. BOX 608, SAN DIEGO 12, CALIFORNIA

GA-5119

**SUMMARY REPORT**  
**ON THE THEORY OF HYPERVELOCITY IMPACT**

J. M. Walsh, W. E. Johnson, J. K. Dienes,  
J. H. Tillotson, and D. R. Yates

Advanced Research Projects Agency  
ARPA Order No. 71-62  
Ballistic Research Laboratories  
Army Contract DA-04-495-AMC-116(X)

March 31, 1964

## ABSTRACT

This study is devoted primarily to solid-solid impact at velocities in the meteoric range. A continuous Eulerian hydrodynamic code is used to numerically integrate the flow equations for several series of impact problems. The impact velocity, the projectile shape, the density of the projectile, and the equation of state of the interacting materials are varied. Impact crater dimensions are found to increase as the 0.58 power of the impact velocity. Projectiles of the same mass but different densities have the same overall impact effects on the target, for velocities above about  $10^6$  cm/sec.

One-dimensional and axisymmetric impacts are also computed for materials with an ideal-gas equation of state. These calculations provide some important comparisons with analytical work on the problem of hypervelocity impact.

Many of the concepts used in solid-solid impact are already present in the one-dimensional problem. The theory for this well-understood impact is discussed in considerable detail.

## CONTENTS

ABSTRACT .....	i
1. INTRODUCTION AND SUMMARY .....	1
2. GOVERNING EQUATIONS AND UNDERLYING APPROXIMATIONS .....	4
3. EQUATION OF STATE .....	6
4. HYDRODYNAMIC CODES .....	8
5. ONE-DIMENSIONAL IMPACT WITH IDEAL-GAS EQUATION OF STATE .....	14
5.1. Mathematical Analysis of Similarity Flow .....	15
5.2. Physical Interpretation of Similarity Flow .....	19
6. AXISYMMETRIC IMPACT WITH IDEAL-GAS EQUATION OF STATE .....	27
7. HYDRODYNAMICS OF SOLID-SOLID IMPACT .....	37
7.1. Dimensional Analysis and Late-stage Equivalence .....	37
7.2. General Comments on a Typical Problem .....	39
7.3. Velocity Late-stage Equivalence .....	43
7.4. Material Equivalence .....	48
7.5. Projectile-shape Effects .....	52
7.6. Density-effect Studies .....	55
8. OVERALL EFFECTS OF SOLID-SOLID IMPACT .....	58
8.1. Penetration Relation .....	58
8.2. Momentum Multiplication .....	58
8.3. Target-hardness Effects .....	59
9. CONCLUDING REMARKS .....	61
9.1. Principal Conclusions .....	61
9.2. Experimental-Theoretical Correlations .....	62
9.3. Comparison with Other Theoretical Results .....	62
REFERENCES .....	65

## 1. INTRODUCTION AND SUMMARY

The high-velocity impact interaction is separable into an early phase which is governed by the equations of fluid dynamics and a later phase during which material strength, not contained in the fluid dynamics, is no longer a negligible effect.

The present report is devoted primarily to the early fluid-dynamic, or hydrodynamic, phase of the impact interaction. Special emphasis is placed on the property of "late-stage equivalence" within this hydrodynamic phase, whereby it is found that projectiles of differing mass and impact velocity or of various shapes or of unequal densities can give rise to target-plate flows which are very nearly identical after early transient differences have died out.

The property of late-stage equivalence, when it occurs within the hydrodynamic phase of the interaction, is useful because it enables one to circumvent the problem of strength-dependent deformation and to establish the dependence upon the initial conditions of overall impact effects, such as total impulse to the target or target crater size. For example, it is possible to show that an impact in the meteoric velocity range has the same overall effects as a suitable impact at velocities already attained in controlled experiments. Any alternative method of learning the overall effects of impacts at meteoric velocities would involve either treating the strength-dependent deformation problem theoretically or solving the formidable experimental problem of accelerating solid projectiles to these velocities.

The governing equations and the solid equations of state used in this study are given in Sections 2 and 3. In Section 4 the continuous Eulerian hydrodynamic code is described and results for a typical impact problem are compared with those from the same problem done with the particle-in-cell code. The continuous Eulerian version gives a substantially smoother solution which is in good general agreement with integrated or smoothed results from the particle-in-cell code. Furthermore,



the Eulerian code requires considerably less computing time and has been used in almost all of the impact work discussed in this report.

One-dimensional and axisymmetric impacts of materials with ideal-gas equation of state,  $PV = (\gamma - 1)E$ , are discussed in Sections 5 and 6, respectively. The assumption that impacts are late-stage equivalent on the basis of equal  $M_0 v_0^{3\alpha}$ , rather than dependent at late times on the projectile mass,  $M_0$ , and impact velocity,  $v_0$ , individually, is shown to lead to the result that the flow is of the familiar self-similar type. For slab impact and for the special case  $\gamma = 1.4$ , this self-similar flow has been treated analytically in recent years, so that a comparison can be made between the analytical solution and that obtained numerically without the assumption of late-stage equivalence. The numerical solution and the analytical similarity solution are in excellent agreement at late times, and impacts are found to be equivalent on the basis of equal  $M_0 v_0^{1.5}$ , an exponent which is midway between those for equivalence on the basis of equal kinetic energy and equal momentum. Additional considerations indicate that this exponent varies from 1.0 to 1.790 as  $\gamma$  is varied from 1.0 to infinity.

For axisymmetric ideal-gas impact, the similarity solution apparently cannot be obtained analytically without making additional simplifying approximations. But it is possible, from the form of the solution indicated by the assumption of late-stage equivalence, to determine the relation which must exist between the shock attenuation rate and  $\alpha$  and between the rate of increase of selected integrated momenta and  $\alpha$ . These results can be compared with the computed solution, determined without assuming late-stage equivalence. Good agreement is found at late times with the self-similar property of the similarity solution, and the value of  $\alpha$  determined from the shock attenuation and momentum data is  $\alpha = 0.59$ . This  $\alpha$  is to be compared with the value  $1/3$  for momentum equivalence and  $2/3$  for energy equivalence. These results are for  $\gamma = 1.5$  and should therefore apply to solids at extremely high impact velocities because of equation-of-state similarities.

In the case of solid-solid impact, discussed in Section 7, the assumption of late-stage equivalence on the basis of equal  $M_0 v_0^{3\alpha}$  does not lead to the requirement that the solution be expressible as a similarity solution.

The assumption itself, however, is found to be valid at high velocities by comparing computed solutions, and this result can be used to establish overall impact effects. The results of computations for some forty impact interactions are summarized in Section 7. Particular attention is devoted to establishing late-stage equivalence and the limits of its validity, not only in regard to impact velocity variation, but also with respect to changes in projectile shape and equation of state of the impacting solids.

In Section 8 the hydrodynamic equivalence results from Section 7 are used to determine relations for such overall effects as target crater size, total impulse to the target, and the effects of target hardness on crater size. Some concluding remarks are given in Section 9.

The present effort is an extension of the work reported in Ref. 1. This initial study, which was based primarily on the application of a particle-in-cell code to iron-iron impact, is in good general agreement with results given here. The work reported in the present document has been devoted to two main objectives--namely, the development of a more accurate and economical (Eulerian) hydrodynamic code for the treatment of solid-solid impact, and the application of the code to a systematic study of the more important parameters defining an impact interaction. The more significant particle-in-cell impact problems have been redone in order to check the earlier results and the investigations are extended to other materials, to varied projectile shapes, and to unlike-material impact.

It is a pleasure to acknowledge the aid of Dr. Floyd E. Allison of the Ballistic Research Laboratories, who is the technical monitor for this study. We are grateful to Dr. Allison for a number of very helpful discussions of pertinent theoretical and experimental work on the subject of hyper-velocity impact.

## 2. GOVERNING EQUATIONS AND UNDERLYING APPROXIMATIONS

Across shock fronts, the flow satisfies the Rankine-Hugoniot equations

$$\rho_0 u_0 = \rho_1 u_1 ,$$

$$P_0 + \rho_0 u_0^2 = P_1 + \rho_1 u_1^2 ,$$

$$E_1 - E_0 = \frac{1}{2} (P_1 + P_0) (V_0 - V_1) .$$

Elsewhere, the equations for compressible isentropic flow are assumed to apply:

$$\frac{\partial \rho}{\partial t} + \nabla \cdot (\rho \vec{u}) = 0 ,$$

$$\frac{d\vec{u}}{dt} + \nabla P = 0 ,$$

$$\frac{dE}{dt} = - P \frac{dV}{dt} .$$

Here the derivatives  $d/dt$  denote the usual convective derivatives, i. e.,  $df/dt = \partial f/\partial t + \vec{u} \cdot (\nabla f)$ . The set of governing equations is completed by specifying an equation of state, which is conveniently taken to be of the form

$$P = f(\rho, E) .$$

In the present study the equations have been solved numerically by hydrodynamic codes (described in Section 4).

An important property of the above equations is that the solutions can be scaled; i. e., an impact interaction of characteristic length  $L_0$  has the same hydrodynamic solution as an impact of characteristic length  $FL_0$  except that all times and distances are changed by the factor  $F$ ; the

intensive quantities such as pressure, density, and velocity remain unchanged. This scaling property is used in subsequent sections to change the relative size of two impact interactions so that flow configurations are in agreement at late times.

The principal approximations used to derive the governing equations are that viscosity, heat-conduction, radiation, and strength effects within the continuous flow are neglected. Neglecting viscous and heat-conduction terms can be justified for flows of sufficiently large dimensions. Quantitative considerations<sup>(1)</sup> suggest that the effects are negligible for flows of dimensions greater than  $10^{-4}$  or  $10^{-3}$  cm, although there exists considerable uncertainty in this lower limit because the appropriate viscous coefficient for metals is very uncertain. The transport by radiation of a significant fraction of the energy within the interaction is possible only at the very high temperatures associated with impacts around  $3 \times 10^7$  to  $5 \times 10^7$  cm/sec or greater. The exclusion of material strength from the description is possible so long as the stresses are very large compared to the yield strength of the solid. This approximation is valid for early stages of the interaction, but fails at late times. The present treatments of the flow are limited to this early hydrodynamic phase.

The above approximations and the simple scaling law are closely related. Viscous, heat-conduction, and radiation effects would introduce higher-order derivatives in the continuous-flow equations, causing departures from the scaling law. Although strength effects are not important in the hydrodynamic phase, it is pertinent to note (in connection with later estimates of overall impact effects) that ordinary stress-strain effects do scale, whereas time dependence within the stress-strain relation causes a breakdown of simple scaling. Thus the experimental determination that impact effects scale, e. g., that crater size is directly proportional to projectile size or that target impulse varies directly with projectile mass, suggests that the neglected effects do not play an important role in the interaction. Observed departures from such scaling are very important, on the other hand, as evidence that new mechanisms, such as viscous forces or rate-sensitive strength effects, must be included in the equations. The main portion of experimental evidence to date appears to indicate that the simple linear scaling is at least a good approximation.

### 3. EQUATION OF STATE

During the impact interaction, each element of the material is processed by a strong shock wave and is then free to expand isentropically. It is therefore desirable to have an equation-of-state representation which accurately reproduces both the Hugoniot curve and expansion isentropes of the material. Such equation-of-state fits for ten common metals and a typical plastic (polyethylene) have been made and described in considerable detail in Ref. 2. The input data for the fits consist of available experimental shock-wave results, usually extending to a few megabars, and of theoretical equation-of-state results by Cowan from the Thomas-Fermi-Dirac model of the atom, for pressures of several tens of megabars and greater. For condensed states, the equation of state is

$$P = \left[ a + \frac{b}{\frac{E}{E_0 \eta^2} + 1} \right] \frac{E}{V} + A\mu + B\mu^2,$$

and for expanded states, the pressure is given by

$$P = aE\rho + \left[ \frac{bE\rho}{\frac{E}{E_0 \eta^2} + 1} + A\mu e^{-\beta(V/V_0 - 1)} \right] e^{-\alpha(V/V_0 - 1)^2},$$

where  $P$  is pressure,  $E$  is specific internal energy,  $\rho$  is density ( $\rho = 1/V$ ), and  $\eta = \rho/\rho_0$ ,  $\mu = \eta - 1$ . The remaining parameters are chosen to fit the equation-of-state data for the individual materials. Values of these parameters for the eleven materials are given in Table 1.

For the calculations in this study, the condensed form of the equation of state has been used for states  $V/V_0 < 1$  and for all states  $E < E_s$  and the expanded form of the equation of state is used for  $V/V_0 > 1$  and  $E > E_s$ . This definition of regions for the condensed and expanded formulations is slightly different from that given previously, the change having been made

to avoid an artificial vaporization of highly expanded, but cold, debris. Finally, negative pressures which may arise in the condensed formulation have been set to zero in the calculations, except in two problems where the effects of this simplification were explored.

Table 1  
EQUATION-OF-STATE CONSTANTS

Material	a	b	$\rho_0$	$E_0$ (Mb-cm <sup>3</sup> /g)	A (Mb)	B (Mb)	$E_s$ (Mb-cm <sup>3</sup> /g)	$\alpha$	$\beta$
CH <sub>2</sub>	0.6	2.0	0.92	0.07	0.075	0.02	0.024	10	5
Pb	0.4	2.37	11.34	0.015	0.4664	0.15	0.0026	13	15
W	0.5	1.04	19.17	0.225	3.08	2.50	0.014	10	10
Cu	0.5	1.5	8.90	0.325	1.39	1.10	0.02	5	5
Fe	0.5	1.5	7.86	0.095	1.279	1.05	0.025	5	5
Al	0.5	1.63	2.70	0.050	0.752	0.65	0.03	5	5
Be	0.55	0.62	1.85	0.175	1.1734	0.55	0.10	5	5
Ti	0.5	0.60	4.50	0.070	1.03	0.50	0.035	5	5
Ni	0.5	1.33	8.86	0.090	1.912	1.50	0.03	5	5
Mo	0.5	1.02	10.20	0.045	2.713	1.65	0.03	5	5
Th	0.4	0.86	11.68	0.025	0.531	0.50	0.02	9	0.88

#### 4. HYDRODYNAMIC CODES

An excellent general description of the particle-in-cell method is to be found in the original Los Alamos Scientific Laboratory literature.<sup>(3,4)</sup> Two similar particle-in-cell codes, SHELL and SPEAR, are operative at General Atomic, and the continuous Eulerian code uses, insofar as possible, the general scheme found in SHELL.<sup>(5)</sup>

A central notion in all of these codes is the division of space into cells which remain fixed and through which the fluid moves. Each cell, at time  $t$ , has associated with it values of the fluid density, total fluid energy, and the components of velocity of the fluid. The process of advancing the dependent variables to time  $t + \Delta t$  is done in two distinct phases. In Phase I, the field terms in the equations, all involving pressure, are used to partially update the dependent variables, with the remaining transport terms being neglected. In Phase II, the transport terms are accounted for in a process which involves moving material across cell boundaries. Finally, new cell pressures are computed from the updated densities and energies and the time step for the next cycle is determined.

The continuous Eulerian and the particle-in-cell codes differ in the procedure used for the Phase II material transport. In the particle-in-cell scheme, each particle represents a finite mass so that very small variations in cell density are not accurately reproduced. The solutions obtained with the particle-in-cell code exhibit unreal cell-to-cell fluctuations, but integrated or suitably averaged quantities appear to be reliable. The continuous Eulerian code, on the other hand, permits small variations in cell density and rarefaction to very small densities. A disadvantage to the Eulerian scheme is the loss of the Lagrangian aspects of the particle scheme. Elements of mass are no longer individually identified from cycle to cycle, and the location of material interfaces and material free surfaces also offers special problems. In the present effort, special restrictions on the transport have been used to prevent the artificial smearing out of solid free surfaces, and applications of the Eulerian code have so far been limited to like-material impacts.

A number of problems have been computed in the process of developing the continuous Eulerian code, and the results have been compared with available analytical solution and with computed results from the SHELL and SPUTTER (one-dimensional Lagrangian) hydrodynamic codes. Flows treated include the shock-tube problem, the one-dimensional rarefaction to zero pressure, the spherical blast problem, and a number of plane and axisymmetric impact interactions. In general, these comparisons have been quite encouraging, with good agreement being found between the continuous Eulerian results and the analytical or SPUTTER solutions. The particle-in-cell and continuous Eulerian results are also in good general agreement, with the former solution being relatively free from undesirable oscillations. The most extensive comparison of the particle-in-cell and continuous Eulerian codes has been for the axisymmetric impact problem described in the following paragraphs.

An iron projectile, a right circular cylinder 3 cm long by 3 cm diameter, impinges on a semi-infinite iron target at a velocity of  $4 \times 10^6$  cm/sec. The problem was run using both the continuous Eulerian and the particle-in-cell codes. The grid size and starting conditions were identical for both problems, with 72 cells in the pellet and 2976 cells in the target. Cell dimensions were 0.25 cm and the particle code used 16 particles/cell.

Representative comparisons of results from the continuous Eulerian and particle codes are given in Figs. 1, 2, and 3. Figure 1 is a plot of momentum versus time data for the two problems. Here the axial momentum  $\sum M_i v_i$  is the momentum in the original pellet flight direction summed over all material with a positive component of velocity in that direction. Similarly, the radial momentum  $\sum M_i u_i$  is an integrated momentum for the radial motion and is summed over all material above the initial target-projectile interface and for which the radial velocity is positive. The agreement between momentum results from the two codes is seen to be remarkably good.\*

Figures 2 and 3 are plots of pressure, compression, and velocity profiles from the two codes at successive times and along a column of

---

\* These momenta have proved useful as accurate measures of the total target disturbance and are used elsewhere in this report.



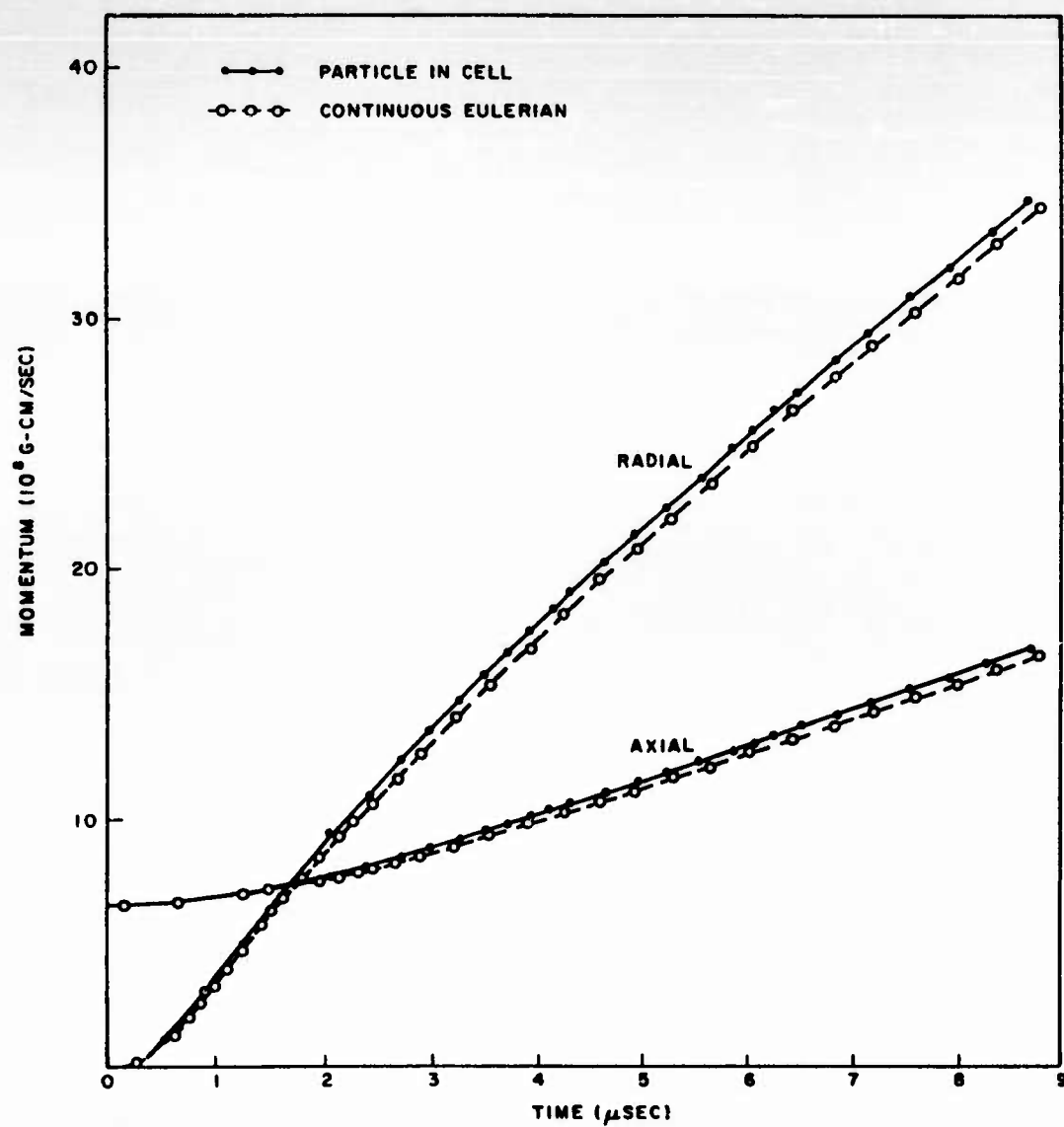


Fig. 1--Comparison of radial and axial momenta from the particle-in-cell and continuous Eulerian codes

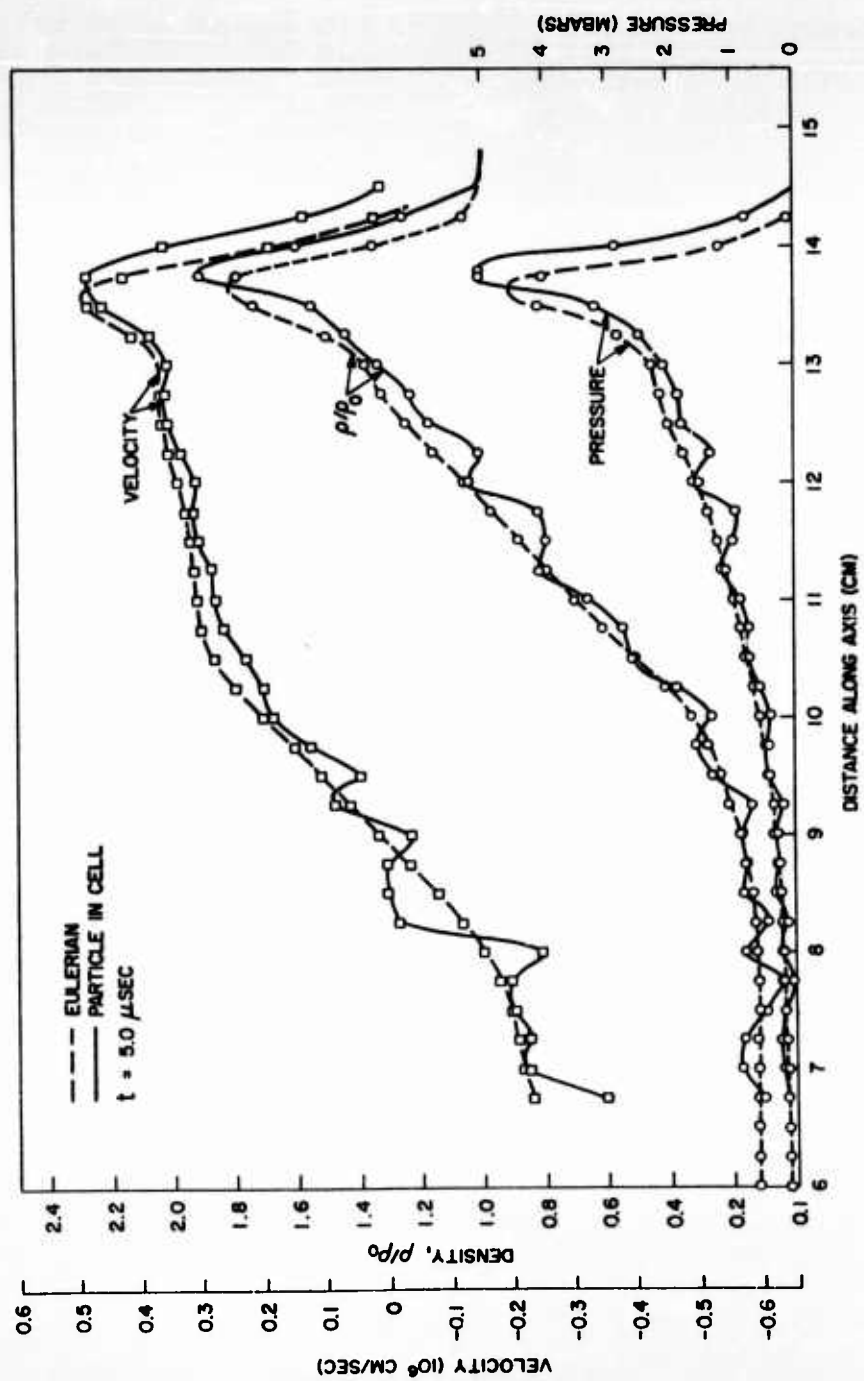


Fig. 2--Comparison of axial velocity, compression, and pressure profiles from the particle-in-cell and continuous Eulerian codes

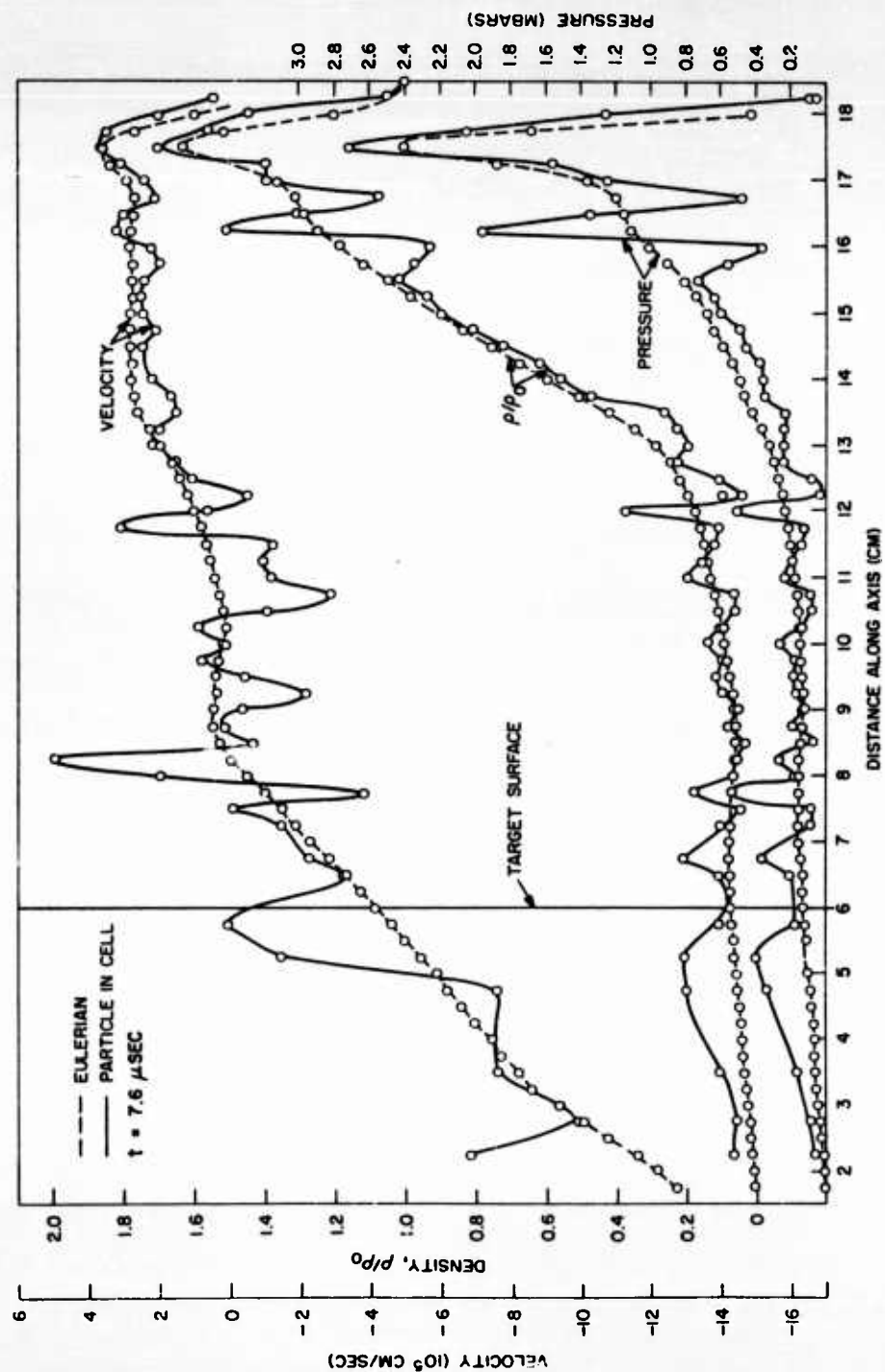


Fig. 3--Comparison of axial velocity, compression, and pressure profiles from the particle-in-cell and continuous Eulerian codes

cells near the axis of symmetry. The results given here are typical of those which have been obtained in a number of such comparisons: The continuous Eulerian solution is relatively smooth and in good general agreement with the particle-in-cell results, the cell-to-cell fluctuations in the latter being attributed to the approximate mass resolution. The fluctuations are more pronounced at the later time owing to the necessity of defining smaller compressions.

The particle-in-cell code in the above comparison required longer machine time by a factor of 15, the additional time being consumed in processing data for the individual particles.

A more detailed description of the continuous Eulerian code is planned by W. E. Johnson.

## 5. ONE-DIMENSIONAL IMPACT WITH IDEAL-GAS EQUATION OF STATE\*

The flow resulting from the impact of a slab on a semi-infinite target contains many of the essential elements of three-dimensional impact theory and yet is amenable to a relatively simple analytical treatment provided the target and slab are both taken to have an ideal-gas equation of state and to be devoid of internal energy prior to impact. In addition, it is possible to obtain very accurate solutions to the flow equations by numerical integration using SPUTTER or other hydrodynamic codes.

The first portion of this section contains the formulation of the equations for plane similarity flow based on the notion of late-stage equivalence. The fact that only one projectile parameter,  $L_0 v_0^\alpha$ , is allowed to appear in the problem is sufficient to reduce the general flow equations from a set of partial differential equations to a first-order ordinary differential equation. The value of  $\alpha$  is determined by solving this equation with appropriate boundary conditions.

The second portion of this section makes use of the previous mathematical results to examine the mechanics of the flow. It is shown that the flow has infinite energy and zero momentum, but that the product of energy times momentum to a certain power,  $E l^\lambda$ , is finite. This product is a function of  $L_0 v_0^\alpha$ . In one case where the equations can be solved exactly,  $\alpha$  is found to be  $3/2$ . In this case, it is shown that it is correct to equate the  $E l^\lambda$  product for the similarity flow to the value of  $E_0 l_0^\lambda$  of the slab. In general,  $\alpha$  depends on the equation of state chosen. For a perfect gas,  $\alpha$  is obtained as a function of  $\gamma$  by interpreting the work of previous authors in terms of the concept of late-stage equivalence.

---

\* This section is essentially self-contained. It can be read separately from the rest of the report and can be skipped in a first reading of the report.

### 5.1. MATHEMATICAL ANALYSIS OF SIMILARITY FLOW

The analysis of the flow is most conveniently discussed by formulating the Lagrangian equations of motion. Let  $h$  denote the number of grams per square centimeter separating a particle from the free surface at  $h = 0$ ,  $u(h, t)$  be the velocity of the particle specified by  $h$ ,  $p$  is the pressure,  $V$  is the specific volume, and  $V_0$  its initial value. It follows that the initial distance of a particle from the free surface is  $hV_0$ . The equations of motion can then be written:<sup>(6)</sup>

$$\dot{V} = u_h \quad (\text{conservation of mass}) , \quad (1)$$

$$\dot{u} = -p_h \quad (\text{conservation of momentum}) , \quad (2)$$

$$p = f(h)V^{-\gamma} \quad (\text{isentropic expansion}) . \quad (3)$$

The boundary conditions for the flow at the shock front are the Rankine-Hugoniot relations. These are reproduced below for a target that is a perfect gas with no initial internal energy:

$$p_s = \frac{2}{\gamma + 1} \frac{v_s^2}{V_0} , \quad (4)$$

$$V_s = \frac{\gamma - 1}{\gamma + 1} V_0 , \quad (5)$$

$$v_s = \frac{\gamma + 1}{2} u_s . \quad (6)$$

The subscript  $s$  denotes the value of any quantity at the shock front and  $v_s$  is the shock velocity. In addition, the pressure must vanish on the free surface.

The independent variables of the problem are  $h$  and  $t$ , but the principle of late-stage equivalence leads to the conclusion that  $h$  can only appear with  $V_0$ ,  $L_0$ , and  $v_0$  in the nondimensional combination

$$L_0 v_0^\alpha \frac{t^\alpha}{(hV_0)^{\alpha+1}} .$$

It is natural to choose as a similarity variable,  $\eta$ , the ratio of  $h$  to its value at the shock front,  $h_s(t)$ . This approach can be reconciled with late-stage equivalence by determining  $h_s(t)$  from the equation

$$\eta = \frac{h}{h_s(t)} = \frac{1}{\theta} \left[ \frac{L_0 v_0^\alpha t^\alpha}{(h v_0)^{\alpha+1}} \right]^{-1/(\alpha+1)}, \quad (7)$$

where  $\theta$  is an undetermined constant. The position of the shock is then given explicitly by

$$h_s(t) = \theta (L_0 v_0^\alpha t^\alpha)^{1/(\alpha+1)} / v_0. \quad (8)$$

If a similarity solution exists and late-stage equivalence holds, then the pressure, velocity, and specific volume must have the form

$$p = \theta_1 \frac{(L_0 v_0^\alpha)^{2/\alpha}}{v_0^{1+2/\alpha}} \frac{\bar{p}(\eta)}{h_s^{2/\alpha}}, \quad (9)$$

$$u = \theta_2 \frac{(L_0 v_0^\alpha)^{1/\alpha}}{v_0^{1/\alpha}} \frac{\bar{u}(\eta)}{h_s^{1/\alpha}}, \quad (10)$$

$$V = \theta_3 v_0 \bar{V}(\eta), \quad (11)$$

where  $\theta_1$ ,  $\theta_2$ , and  $\theta_3$  are constants and the barred variables are non-dimensional functions defined to be unity at the shock front, i.e.,

$$\bar{p}(1) = \bar{u}(1) = \bar{V}(1) = 1. \quad (12)$$

In order that the Rankine-Hugoniot conditions be satisfied at the shock, it is necessary that

$$\theta = \left( \frac{\gamma+1}{2} \frac{\alpha+1}{\alpha} \theta_2 \right)^{\alpha/(\alpha+1)}, \quad (13)$$

$$\theta_1 = \frac{\gamma+1}{2} \theta_2^2, \quad (14)$$

$$\theta_3 = \frac{\gamma-1}{\gamma+1}. \quad (15)$$

The similarity assumption inherent in Eqs. (9), (10), and (11) reduces the flow equations to the following second-order system of ordinary differential equations for  $\bar{p}$ ,  $\bar{u}$ , and  $\bar{v}$ :

$$\eta \bar{u}' + \bar{u}/\alpha = \bar{p}', \quad (16)$$

$$\bar{u}' + \frac{\gamma-1}{2} \eta \bar{v}' = 0, \quad (17)$$

$$\eta^{2/\alpha} \bar{p} \bar{v}^\gamma = 1. \quad (18)$$

These equations can be solved for the derivatives  $\bar{p}'$ ,  $\bar{u}'$ , and  $\bar{v}'$ :

$$\bar{p}' = -\frac{2}{\alpha} \frac{\bar{p}}{\eta} \frac{1 + \frac{\gamma}{\gamma-1} \frac{\bar{u}}{\eta \bar{v}}}{1 - \frac{2\gamma}{\gamma-1} \frac{\bar{p}}{\eta^2 \bar{v}}}, \quad (19)$$

$$\bar{v}' = \frac{1}{\alpha} \frac{2}{\gamma-1} \frac{\bar{u}}{\eta^2} \frac{1 + \frac{2\bar{p}}{\eta \bar{u}}}{1 - \frac{2\gamma}{\gamma-1} \frac{\bar{p}}{\eta^2 \bar{v}}}, \quad (20)$$

$$\bar{u}' = -\frac{\bar{u}}{\alpha \eta} \frac{1 + \frac{2\bar{p}}{\eta \bar{u}}}{1 - \frac{2\gamma}{\gamma-1} \frac{\bar{p}}{\eta^2 \bar{v}}}. \quad (21)$$

Inspection of these equations suggests introducing a new set of variables  $q$  and  $y$ , where

$$q = \frac{2\gamma}{\gamma-1} \frac{\bar{u}^2}{\bar{p} \bar{v}} = M^2 \gamma^2, \quad (22)$$

$$y = \eta \bar{u} / \bar{p}, \quad (23)$$

and  $q$  is proportional to the square of the local Mach number,  $M$ . After some calculation, one finds the following first-order equation for  $q(y)$ :

$$\frac{dq}{dy} = \frac{q}{y} \frac{-4y + \left(\frac{\gamma-1}{\gamma} y - \frac{2}{\gamma}\right)q}{(1+\alpha)y^2 - 2y + (y-\alpha)q}. \quad (24)$$



The choice of variables given by Eqs. (22) and (23) was suggested by M. Nowak<sup>(7)</sup> and results in a somewhat simpler equation than given by previous authors. The solution must satisfy the boundary condition

$$q(1) = \frac{2\gamma}{\gamma - 1} . \quad (25)$$

Furthermore, the pressure must vanish at the free surface. In terms of the present variables, this requires that the behavior of the equations must be determined when the magnitudes of  $q$  and  $y$  are large. It can be shown asymptotically that

$$\frac{q}{y} = - (1 + \alpha)\gamma . \quad (26)$$

Combining this result with Eqs. (19) and (21) provides the required behavior of the pressure and velocity at the free surface:

$$\bar{p} \sim \eta^{(2/\alpha)[(\gamma/2)-1]+\gamma} , \quad (27)$$

$$u \sim \eta^{-1/\alpha} . \quad (28)$$

This result will be used below.

Equation (24) has a saddle point at

$$y = -2, \quad q = 4 , \quad (29)$$

and it can be shown that the solution curve must pass through this singularity. If it does, the pressure vanishes at the free surface and the flow is everywhere well behaved. Thus, the free-surface condition can be replaced by Eq. (29). Equations (25) and (29) together constitute two boundary conditions for the first-order system represented by Eq. (24). It is possible to satisfy both boundary conditions if  $\alpha$  is appropriately chosen and  $\alpha$  is thereby determined. In general, the problem cannot be solved analytically, but numerical approaches have been used by Häfele<sup>(8)</sup> and by Rae and Kirchner<sup>(9)</sup> to solve equations equivalent to Eq. (24). In their analysis a similarity approach based on the parameter  $x/t^n$  was used. Their approach is consistent with the concept of late-stage equivalence. A comparison of the similarity parameter  $x/t^n$  with Eq. (7) shows that

$$\alpha = \frac{n}{1-n} . \quad (30)$$

## 5.2. PHYSICAL INTERPRETATION OF SIMILARITY FLOW

It is possible to plot  $\alpha$  as a function of  $\gamma$ , using the detailed tables of Rae and Kirchner.<sup>(9)</sup> The result is given in Fig. 4. It is found that for  $\gamma$  near one,  $\alpha$  is also near one and impacts are nearly equivalent on a momentum basis.  $\alpha$  increases with  $\gamma$  and asymptotically approaches the value 1.790, so that for no value of  $\gamma$  are flows ever exactly equivalent on an energy basis.

The total energy of the flow to the right of  $h$  is given by the integral

$$E = \int_h^{h_s} \left( \frac{u^2}{2} + \frac{pV}{\gamma - 1} \right) dh \quad (31)$$

and the momentum to the right of  $h$  is given by

$$I = \int_h^{h_s} u \, dh. \quad (32)$$

As  $h$  goes to zero, these quantities approach infinity and zero, respectively. The rate at which these limits are approached is given by substitution from Eq. (28):

$$E \approx h^{1-(2/\alpha)}, \quad (33)$$

$$I \approx h^{1-(1/\alpha)}. \quad (34)$$

From the principle of late-stage equivalence it is expected that the flow should depend only on energy and momentum in a certain combination,  $EI^\lambda$ , where

$$EI^\lambda \approx L_0 v_0^2 \cdot (L_0 v_0)^\lambda = \left[ L_0 v_0^{(2+\lambda)/(1+\lambda)} \right]^{(1+\lambda)}. \quad (35)$$

The relation between  $\lambda$  and  $\alpha$  is thereby determined as

$$\alpha = \frac{2 + \lambda}{1 + \lambda}, \quad \lambda = \frac{2 - \alpha}{\alpha - 1}. \quad (36)$$

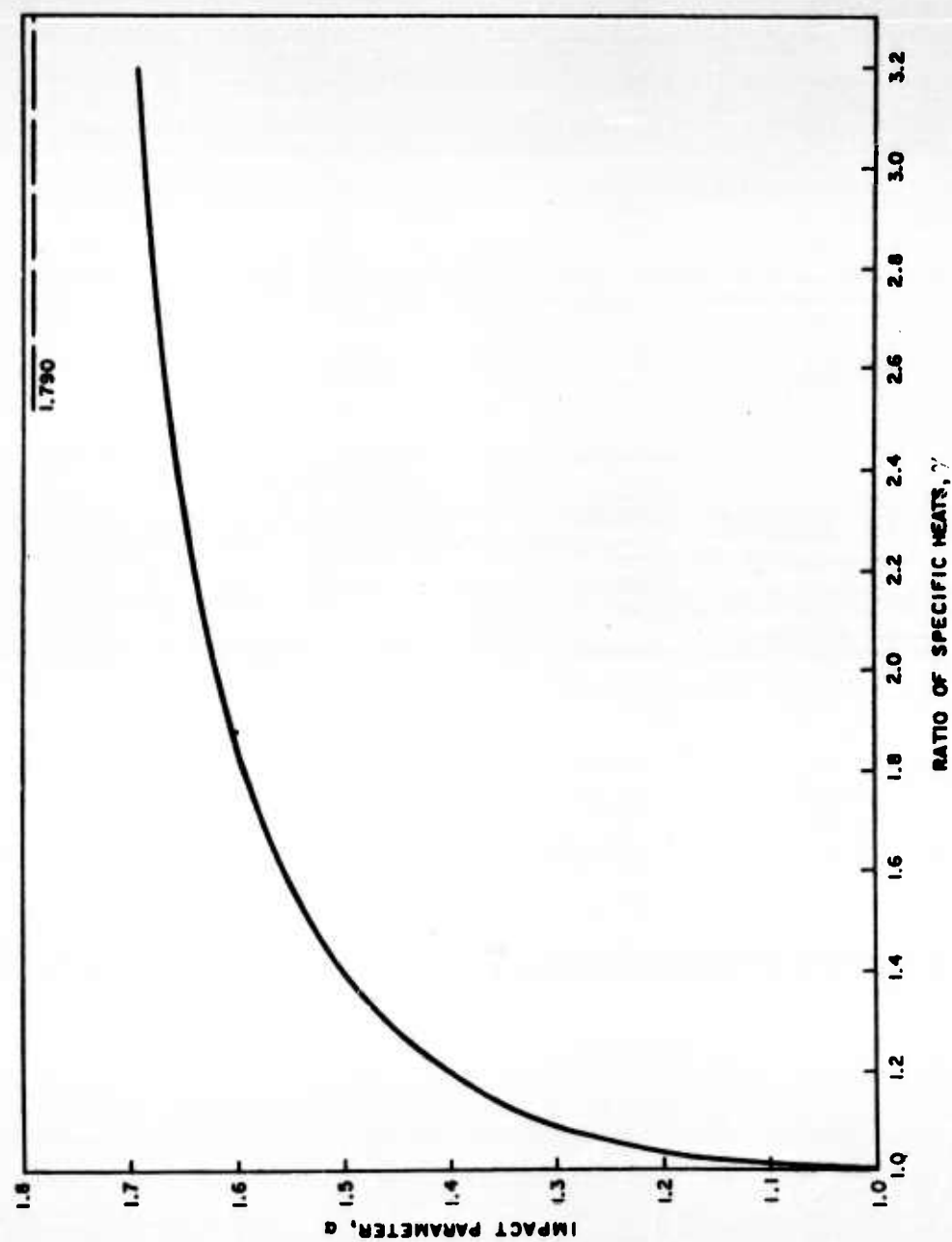


Fig. 4--The impact parameter  $\alpha$  as a function of  $\gamma$  for one-dimensional impact

This consideration suggests that  $EI^{(2-\alpha)/(\alpha-1)}$  obtained from the order of magnitude integrals above should be a finite quantity; that is indeed the case as verified by examining Eqs. (33) and (34).

It seems plausible that the product  $EI^{(2-\alpha)/(\alpha-1)}$  taken over the late-stage flow field should be the same as the product  $L_0 v_0^2 \cdot (L_0 v_0)^{(2-\alpha)/(\alpha-1)/2}$  determined from the energy and momentum of the impacting slab. This cannot be proved without integrating the exact flow equations, which, in general, cannot be done. However, it is possible to carry through the calculations in one particular case. A number of authors have observed that the similarity equations can be integrated if the pressure is linear in  $h$  or, in terms of similarity variables, if  $\bar{p} = \eta$ . This assumption leads to a solution consistent with all the boundary conditions only if  $\gamma = 7/5$  and  $\alpha = 3/2$ , and if so,

$$u = \theta_2 (L_0 v_0^{3/2} / V_0)^{2/3} \bar{u}(\eta) / h_s^{2/3}, \quad (37)$$

where

$$\bar{u}(\eta) = (3 - \eta^{-2/3}) / 2. \quad (38)$$

The asymptotic forms of the energy and momentum integrals are then, for  $\eta$  small,

$$E \approx \frac{3\theta_2^2}{8} \left( \frac{L_0 v_0^{3/2}}{V_0} \right)^{4/3} \frac{1}{h_s^{1/3} \eta^{1/3}}, \quad (39)$$

$$I \approx \frac{3\theta_2}{2} \left( \frac{L_0 v_0^{3/2}}{V_0} \right)^{2/3} h_s^{1/3} \eta^{1/3}. \quad (40)$$

Equating  $EI$  ( $\lambda = 1$  in this case) to the energy-momentum product for the slab determines  $\theta_2$ :

$$\theta_2^3 = 8/9 \quad \text{for } \gamma = 7/5. \quad (41)$$

EI may be thought of as an integral invariant of the flow. This interpretation is strengthened by considering the energy  $E_+$  and momentum  $I_+$  of that portion of the material which is moving in the direction of the original slab. The energy decreases as  $t^{-1/5}$  and the momentum increases as  $t^{1/5}$ . However, the product  $E_+ I_+$  is constant and equal to 0.5132 of the product taken over the entire flow.

To verify this hypothesis that the EI product for the slab and the similarity flow are equal, a numerical integration of the flow equations was carried out using the SPUTTER code. This has also provided an example of how rapidly the flow approaches the similarity solution. The target material was chosen to have a density of one; the velocity of the projectile was taken to be  $10^6$  cm/sec; and the mass per unit area,  $h_0 = L_0/V_0$ , was taken to be  $1.2 \text{ g/cm}^2$ . At impact the shock strength was 0.3 Mbar.

Pressure, velocity, and density data obtained from the computer solution are presented in Figs. 5, 6, and 7 and are compared with the analytical solution at corresponding times. In the figures, time is given from the instant of contact in the finite-slab solution. The appropriate time origin for the analytical solution is the instant of impact by a slab of zero thickness and is found by subtracting  $0.88 \mu\text{sec}$  from the numbers that are given. All data points obtained from the SPUTTER code solution in the neighborhood of the shock are shown. However, only representative data points are given where the oscillations found near the shock front have died out. No attempt was made to optimize the quality of the computer solution, since the agreement with the analytical result is satisfactory. Increase of artificial viscosity in the SPUTTER code would reduce the shock-front oscillations.

These results can be interpreted by considering a family of finite-slab impacts with different values of thickness,  $L_0$ , and velocity,  $v_0$ , subject to the constraint that  $L_0 v_0^\alpha$  is the same for all the slabs. At early times the flow profiles are all quite different, but at late times they all become similar. The thin high-velocity slabs result in flows which approach the similarity flow soonest. In fact, the similarity solution can be interpreted as an impact by a slab of zero thickness and infinite velocity. With the constraint that  $L_0 v_0^\alpha$  is constant, it also follows that the similarity solution corresponds to impact by a slab with infinite energy

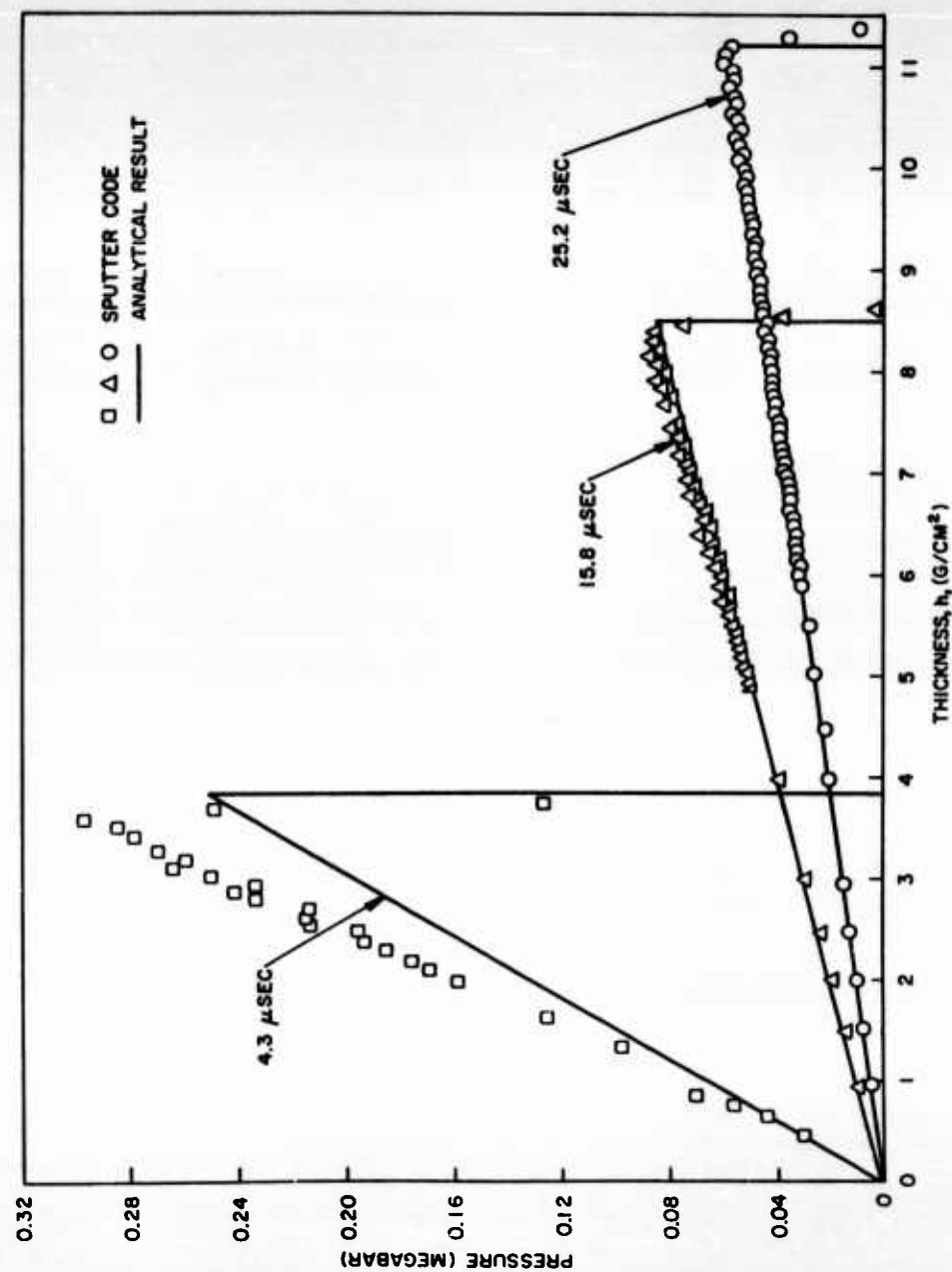


Fig. 5--Comparison of pressure in the finite-slab impact problem with the similarity solution for  $\gamma = 7/5$  at three times;  $h$  is measured from the free surface

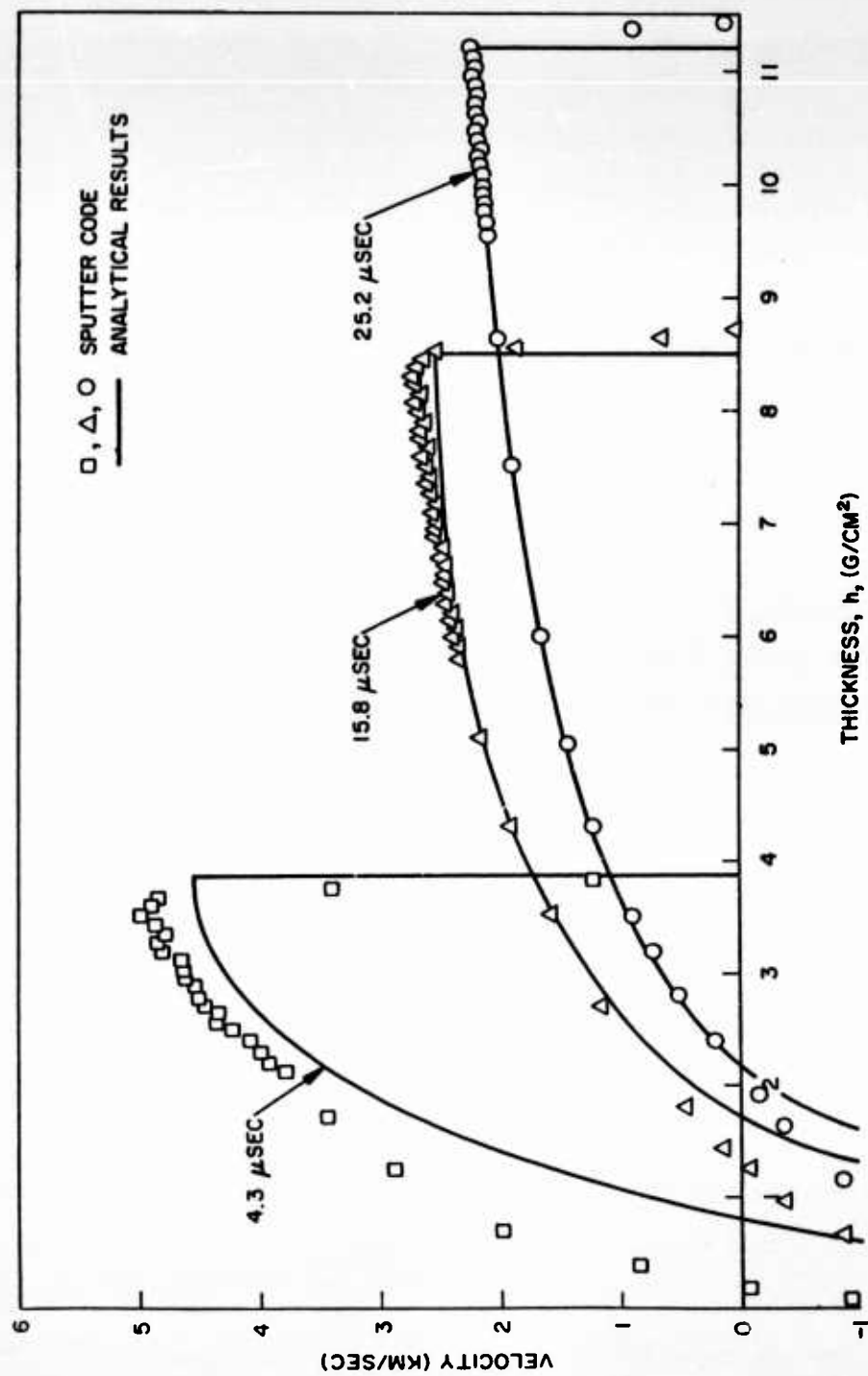


Fig. 6--Comparison of velocity in the finite-slab impact problem with the similarity solution for  $\gamma = 7/5$  at three times;  $h$  is measured from the free surface

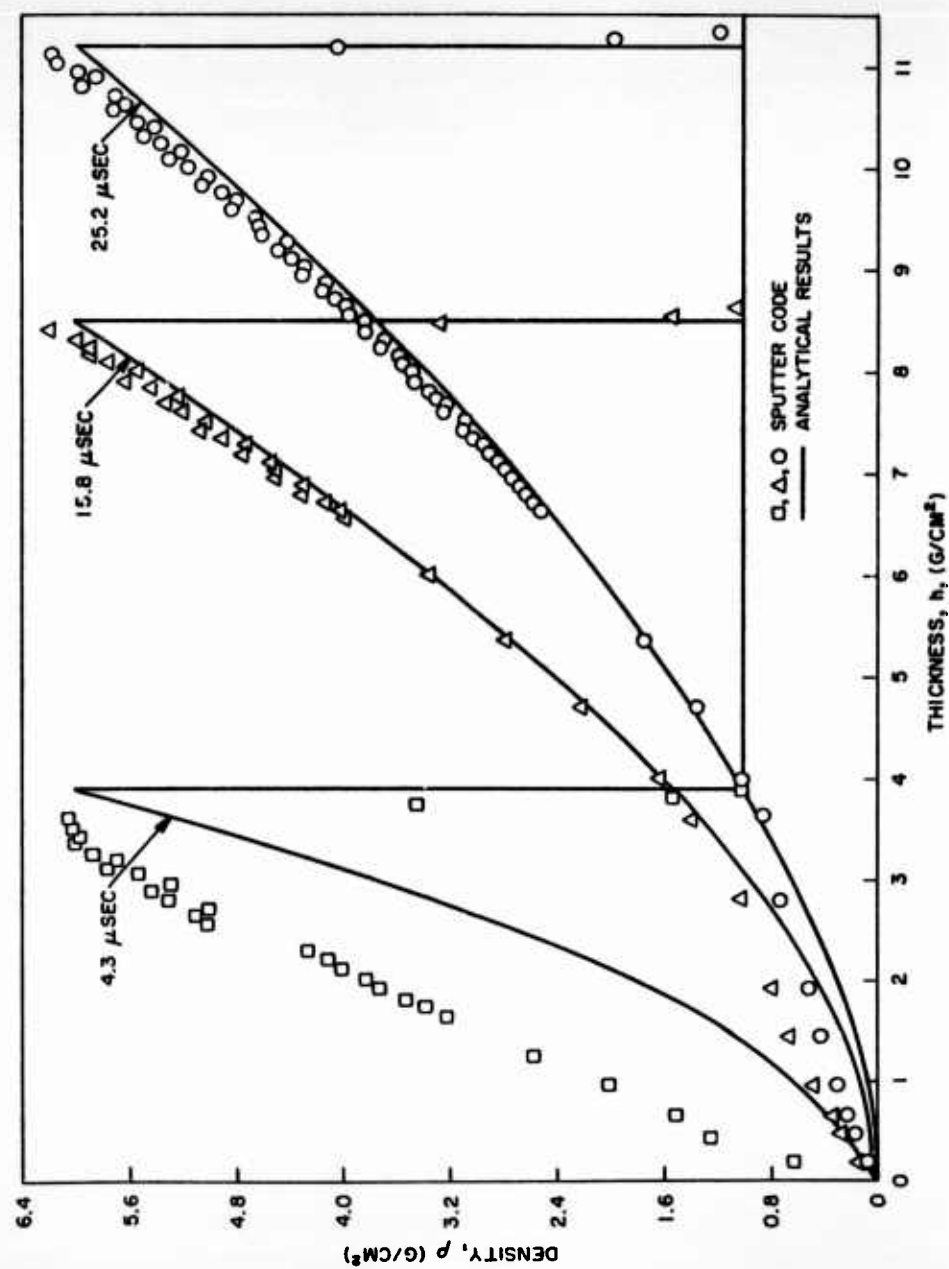


Fig. 7--Comparison of density in the finite-slab impact problem with the similarity solution for  $\gamma = 7/5$  at three times;  $h$  is measured from the free surface



and zero momentum. Since a similarity solution can contain only one free dimensional parameter, in this case  $L_0 v_0^\alpha$ , the energy and momentum of the impacting slab cannot both be reconstructed from looking at the late-stage similarity flow. However, the product  $E I^{(2-\alpha)/(\alpha-1)}$  is characteristic of the impact and reflects the dependence of the flow on the initial momentum and energy of the slab.

## 6. AXISYMMETRIC IMPACT WITH IDEAL-GAS EQUATION OF STATE

The impact behavior of an initially cold ideal-gas material is a considerably simpler problem than that of solids because the effect of variation in impact velocity can be determined from dimensional considerations alone. Thus, it is necessary to solve the problem for only one impact velocity for each  $\gamma$  and initial geometry.

For a given geometry, say that of a sphere or cylindrical pellet on a semi-infinite plate, the problem is fully characterized by given values of  $\gamma$ , the initial density,  $\rho_0$ , the size (a length  $L_0$ ) of the projectile, and the impact velocity,  $v_0$ . From the usual dimensional considerations, therefore, the solution must be of the form

$$\rho = \rho_0 f_1 \left( \frac{r}{L_0}, \frac{z}{L_0}, \frac{tv_0}{L_0}, \gamma \right),$$

$$P = \rho_0 v_0^2 f_2 \left( \frac{r}{L_0}, \frac{z}{L_0}, \frac{tv_0}{L_0}, \gamma \right),$$

$$u = v_0 f_3 \left( \frac{r}{L_0}, \frac{z}{L_0}, \frac{tv_0}{L_0}, \gamma \right),$$

$$v = v_0 f_4 \left( \frac{r}{L_0}, \frac{z}{L_0}, \frac{tv_0}{L_0}, \gamma \right),$$

where  $r$  and  $z$  are cylindrical coordinates with origin at the center of impact on the target free surface. Thus, the variation of  $\rho_0$  causes only a proportional change in the densities and pressures and the effect of varying  $v_0$  is only to change the time, pressure, and velocity scales in a manner which is easily determined by inspection of the above expressions.

Additional simplification of the solution can be attained if we introduce the assumption of late-stage equivalence. The assumption is suggested by studies of solid-solid impact, where it has been found that impacts at different velocities, though different at early times, rapidly become very nearly the same, provided the relative scale of the two impacts is such that  $L_0 v_0^\alpha$  is constant. The analytical statement of this assumption is to require that the solution not contain  $L_0$ ,  $v_0$  as individual parameters, but only in the combination  $L_0 v_0^\alpha$ , where  $\alpha$  is a constant to be determined. It follows directly that the solution must approach at late times a flow expressible in the form

$$\rho = \rho_0 g_1 \left( \frac{R^{\alpha+1}}{\tau^\alpha}, \frac{Z^{\alpha+1}}{\tau^\alpha}, \gamma \right),$$

$$P = \rho_0 v_0^2 Z^{2/\alpha} g_2 \left( \frac{R^{\alpha+1}}{\tau^\alpha}, \frac{Z^{\alpha+1}}{\tau^\alpha}, \gamma \right),$$

$$u = v_0 Z^{-1/\alpha} g_3 \left( \frac{R^{\alpha+1}}{\tau^\alpha}, \frac{Z^{\alpha+1}}{\tau^\alpha}, \gamma \right),$$

$$v = v_0 Z^{-1/\alpha} g_4 \left( \frac{R^{\alpha+1}}{\tau^\alpha}, \frac{Z^{\alpha+1}}{\tau^\alpha}, \gamma \right),$$

where

$$\tau = t v_0 / L_0, \quad R = r / L_0, \quad Z = z / L_0.$$

Thus the assumption of late-stage equivalence leads one to a similarity solution; i.e., the number of independent variables in the functions is reduced to two instead of the original three.

The reduction to two variables still leaves one, however, with a set of partial differential equations, and the flow is presumably not amenable to analytical solution without additional approximations. It is possible, however, to draw certain physical conclusions from the form of the late-stage solution:

1. The flow configuration is asymptotically self-similar. The compression  $\rho/\rho_0$ , for example, is the same at corresponding points (equal  $Z\alpha+1/\tau\alpha$ ,  $R\alpha+1/\tau\alpha$ ). Pressures at corresponding points are in the ratio  $(Z_1/Z_2)^{-2/\alpha}$ , where  $Z_1/Z_2$  is the ratio of the linear dimensions of the configuration at the two times. Similarly, velocities at corresponding points drop off as distance to the  $-(1/\alpha)$  power as the disturbance enlarges.
2. The dimensions of the disturbance increase as  $t^{\alpha/(\alpha+1)}$ .
3. The mass velocity at the shock front and the shock speed attenuate with penetration distance as  $Z^{-1/\alpha}$  or  $t^{-1/(\alpha+1)}$ . The shock pressure attenuates as  $Z^{-2/\alpha}$  or  $t^{-2/(\alpha+1)}$ .
4. The total positive axial and total positive radial momenta increase as  $t^{(3\alpha-1)/(\alpha+1)}$ . This result follows by noting that distances increase as  $t^{\alpha/(\alpha+1)}$ , mass engulfed therefore goes as  $t^{3\alpha/(\alpha+1)}$ , and velocities decrease as  $t^{-1/(\alpha+1)}$ , so that the momentum within corresponding elements of volume varies as  $t^{(3\alpha-1)/(\alpha+1)}$ .

The Eulerian code has been used to treat numerically the problem of a right circular cylinder of unit aspect ratio impacting a semi-infinite target. The value  $3/2$  was chosen for  $\gamma$  because solids at extremely high shock pressures ( $\approx 1,000$  Mbars) have Hugoniot curves and expansion isentropes which approximate those of a  $\gamma = 3/2$  ideal gas. The values  $v_0 = 10^6$  cm/sec,  $\rho_0 = 1$  g/cm<sup>3</sup>, and a projectile diameter of 3.6 cm were used to complete the problem specification.

A point of particular interest concerning the computed solution is whether or not the flow becomes self-similar as indicated by the assumption of late-stage equivalence; after an early phase (two or three times the time required for the initial projectile to move its own length), the flow geometry tends to a configuration which does indeed remain self-similar as it enlarges.

In this late-stage configuration, the shock wave closely approximates a spherical shape, with the (moving) center of the sphere located at about one-third of the shock penetration distance. The target material which has been engulfed by the shock is largely compressed into a thin shell near the shock front. Progressive stages of this flow can be visualized from the velocity and mass flux plots reproduced as Fig. 8.

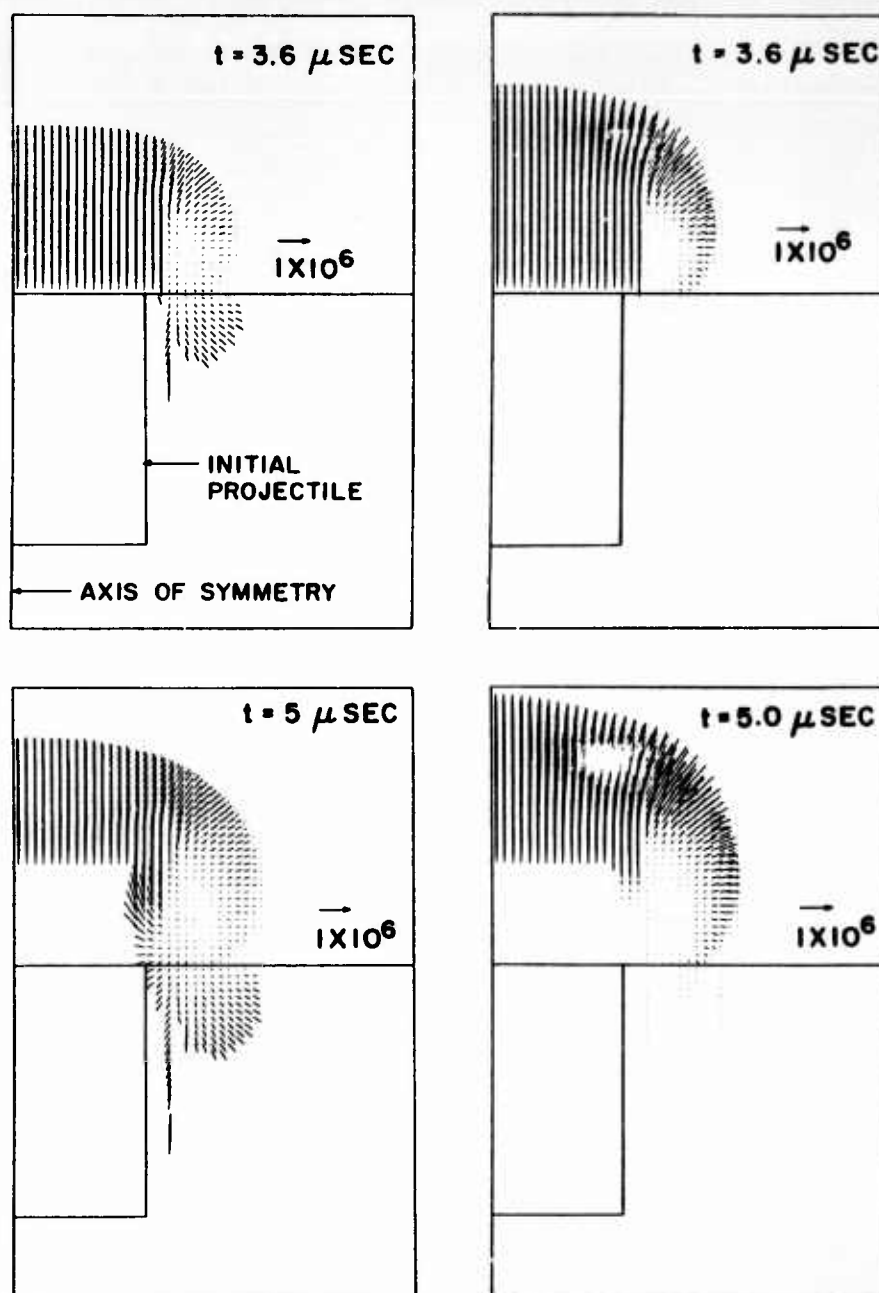


Fig. 8--Velocity (left) and mass flux or momentum (right) vector fields for the axisymmetric gas problem (arrows indicate vector lengths for  $\vec{u} = 10^6 \text{ cm/sec}$  and  $(\rho \vec{u} / \rho_0) = 10^6 \text{ cm/sec}$ )

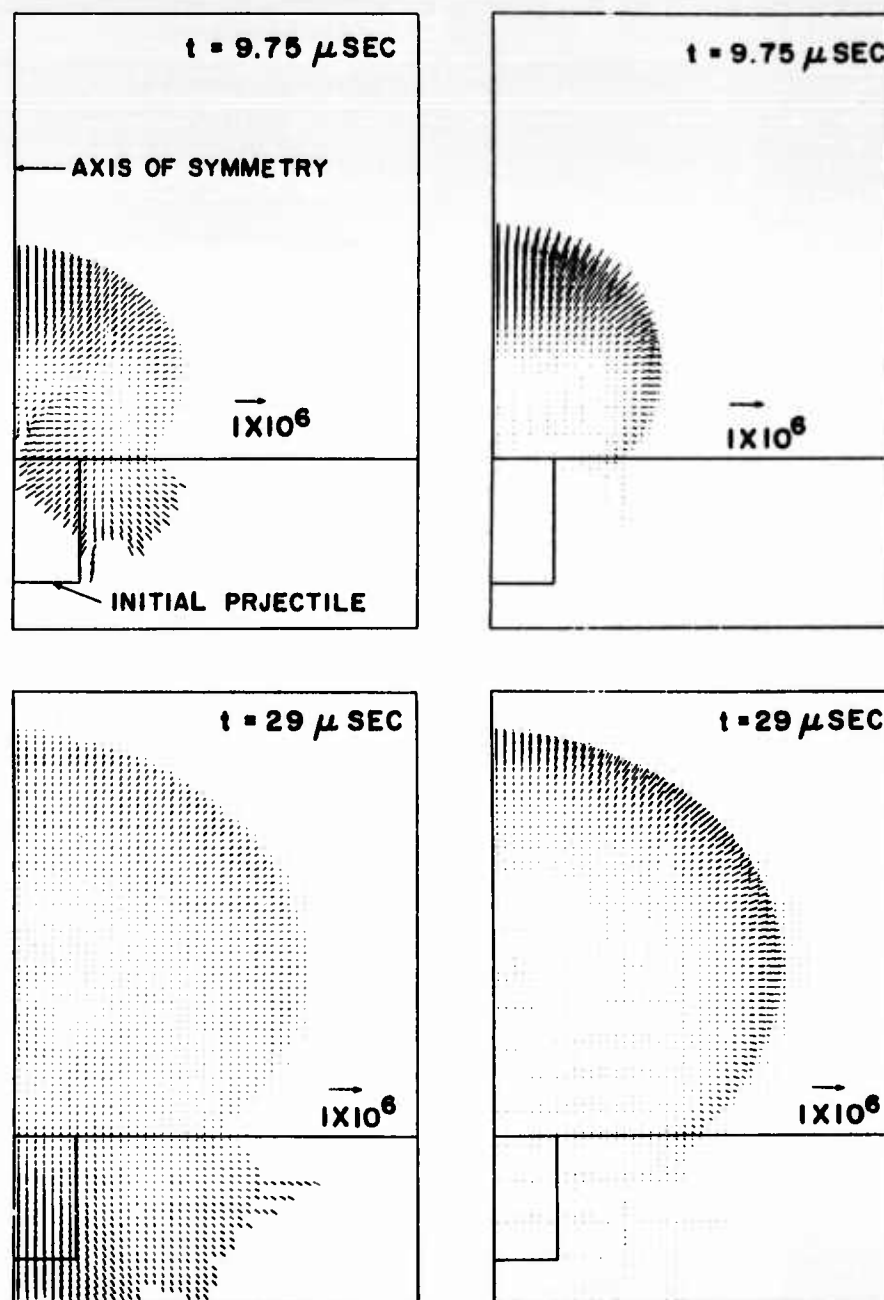


Fig. 8 cont'd--Velocity (left) and mass flux or momentum (right) vector fields for the axisymmetric gas problem (arrows indicate vector lengths for  $\vec{u} = 10^6$  cm/sec and  $(\rho\vec{u}/\rho_0) = 10^6$  cm/sec)

Tests of other flow properties characteristic of the similarity solution, and also determinations of  $\alpha$ , are possible from plots of the integrated momenta and the shock attenuation. Since the momenta must vary as  $t^{(3\alpha-1)/(\alpha+1)}$  if the assumption of late-stage equivalence is valid, one can examine the log-log plots of integrated radial and axial momenta versus time to (a) test if the plots become linear at late times, (b) test whether the late-time slopes of the two momenta plots are in agreement, and (c) determine  $\alpha$  from the slopes. The momentum curves are plotted as Fig. 9, where it is seen that the plots are quite linear at late times and that the slope  $(3\alpha - 1)/(\alpha + 1)$  is in good agreement with both plots if one chooses  $\alpha = 0.59$ . (The slope for  $\alpha = 1/3$  and that for  $\alpha = 2/3$  are indicated on the graph for comparison.) Figure 10 shows log-log plots of shock penetration and shock strength versus time, both for the axis of symmetry. The penetration and attenuation slopes are in reasonable agreement with the values  $\alpha/(\alpha + 1)$  and  $-1/(\alpha + 1)$  using  $\alpha = 0.59$ . (A slightly lower  $\alpha$ , about 0.55, would correlate the results somewhat better; but the value of  $\alpha$  from the momentum curves is considerably more accurate.)

Finally, velocity, density, and pressure profiles at various times can be compared to test whether the flow remains self-similar. The results of a representative comparison--the velocity distributions along  $45^\circ$  for times different by a factor of three--are shown as Fig. 11. It is seen that if the curve for the early time is scaled to a later time by similarity relations  $Z \sim t^{-\alpha/(\alpha+1)}$  and  $v \sim t^{-1/(1+\alpha)}$ , the agreement is good. The value  $\alpha = 0.59$  was used.

The results of all comparisons are, then, compatible with the assumption that the flow has tended to the self-similar form indicated by late-stage equivalence. It is also of interest to note that the value  $\alpha = 0.59$  is in good agreement with the values obtained for condensed materials, despite substantial equation-of-state differences and formal differences in the method of analysis of the numerical results.

Using the assumption that the flow is self-similar, Rae and Kirchner<sup>(9)</sup> have reported some very interesting analytical progress on the problem of axisymmetric ideal-gas impact. By considering the flow equations as specialized to the axis of symmetry and by requiring that the solution pass smoothly through a singularity in the differential equations, they

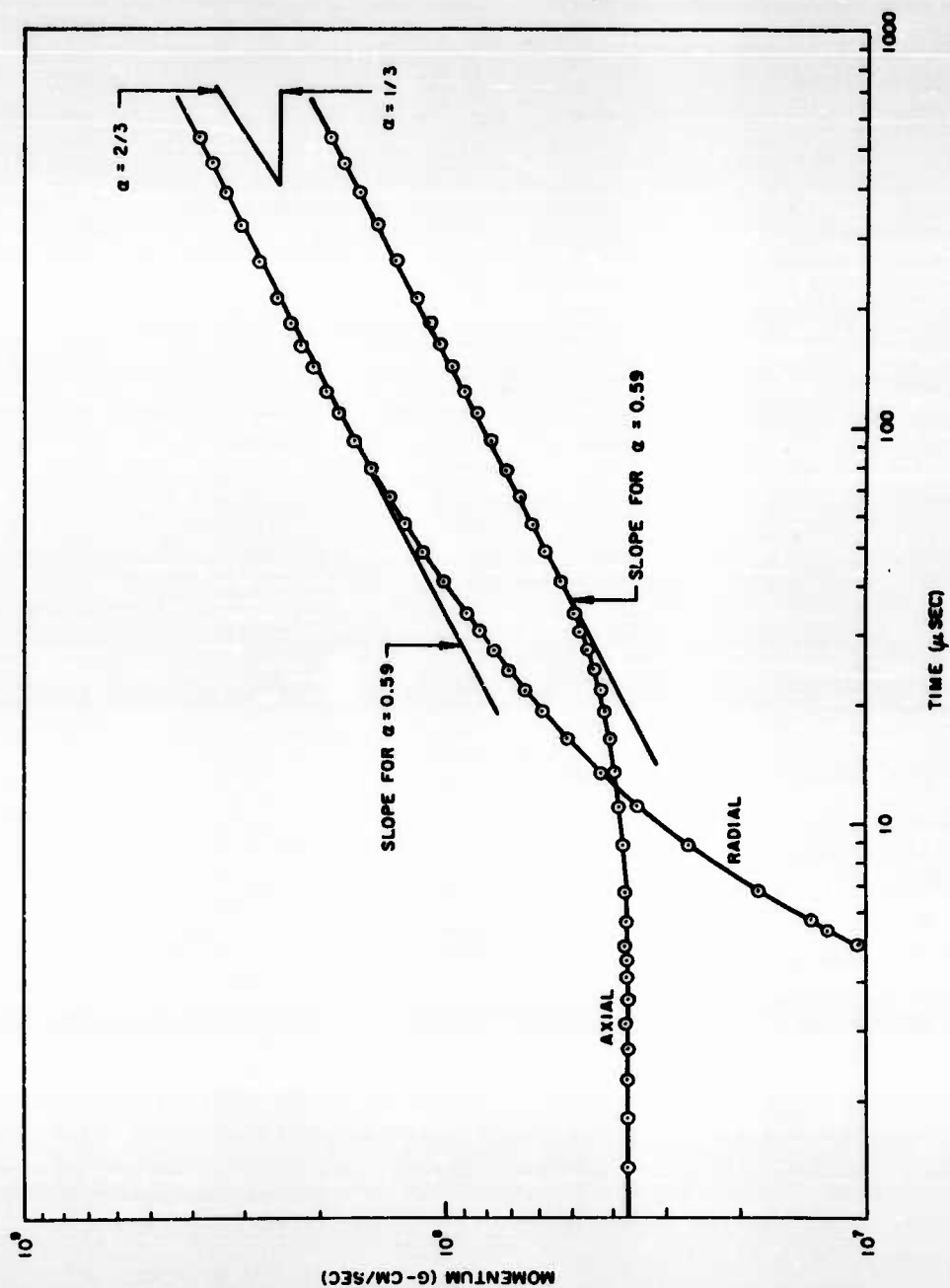


Fig. 9--Radial and axial momenta for the  $\gamma = 1.5$  ideal-gas impact; the slopes necessary for late-stage equivalence on an  $\alpha = 1/3$  and  $\alpha = 2/3$  basis are indicated at the upper right



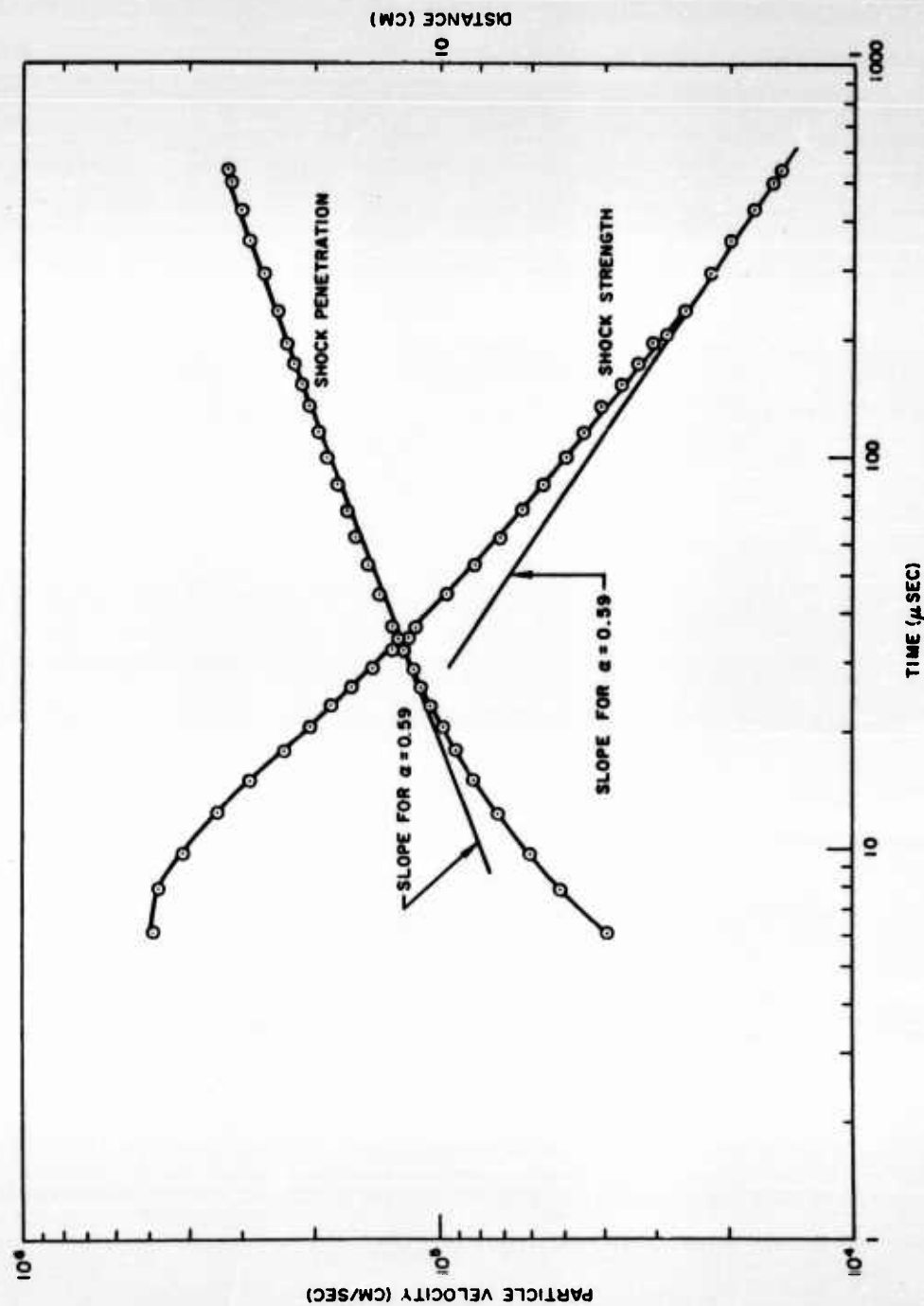


Fig. 10--Shock penetration and shock strength versus time for the  $\gamma = 1.5$  impact

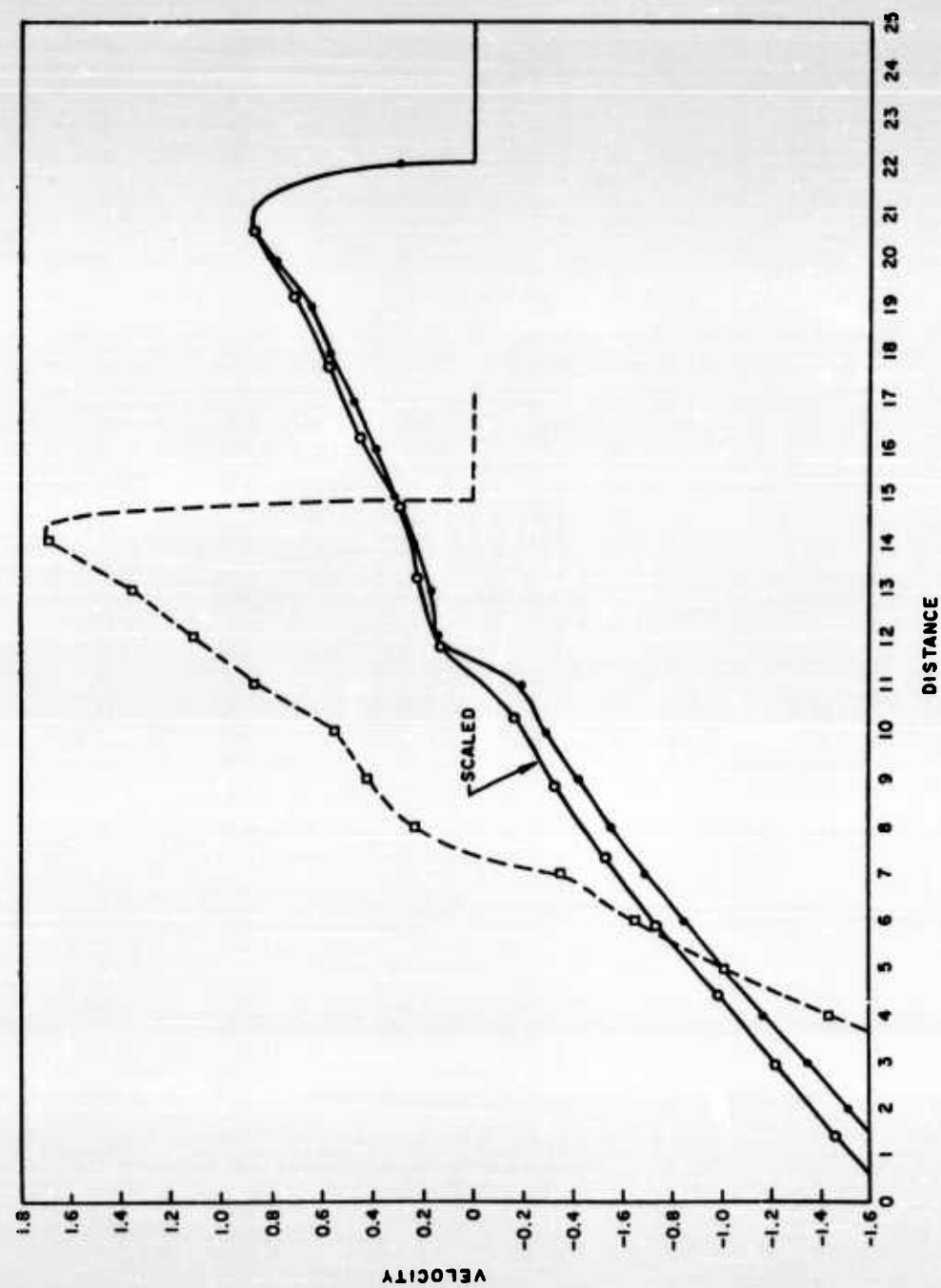


Fig. 11--Velocity versus distance along line 45° from the axis of symmetry; the scaled curve is determined from the earlier data and the similarity relations

find that the exponent  $N$  in the similarity variable  $r/t^N$  can be evaluated to a good approximation.\* Values  $N = 0.37$  to  $0.39$  are obtained, as compared to  $N = 0.40$  for the spherical-blast problem.

A consequence of the late-stage-equivalence interpretation, on the other hand, is a relation between  $\alpha$  and the similarity exponent  $N$ . Specifically, comparison with the present similarity variable  $Z^{\alpha+1}/\tau^\alpha$  shows that  $N = \alpha/(\alpha + 1)$ . Using the present result,  $\alpha = 0.59$ , gives  $N = 0.37$ . Rae gives  $N$  the value  $0.375$  for  $\gamma = 3$  and the value  $0.367$  for  $\gamma = 2$ . Hence, the value for  $\gamma = 3/2$  is found by extrapolation to be  $0.363$ .

The above agreement is, of course, quite gratifying. The numerical integrations and the analytical treatment by Rae and Kirchner<sup>(9)</sup> are based on entirely different approximations, so that the agreement is a significant confirmation of both results.

---

\*The principal approximations, in addition to assuming self-similarity, are: The shock wave in the target is a hemisphere and an estimate is made for the magnitude of  $d^2p/d\theta^2$  at the singular point. The last approximation, and the fact that  $N$  is found to be a weak function of  $\gamma$ , accounts for the small variation in  $N$ .

## 7. HYDRODYNAMICS OF SOLID-SOLID IMPACT

### 7.1. DIMENSIONAL ANALYSIS AND LATE-STAGE EQUIVALENCE

Previous comparisons<sup>(1)</sup> showed that the solid equations of state appropriate to impact work can be correlated by assuming, for simplicity, that two properties, the initial density  $\rho_0$  and the initial sound speed  $c_0 = (\partial P / \partial \rho)_s^{1/2}$ , suffice to characterize a given material. Specifically, the individual equations of state  $P = f(\rho, E)$  of the various metals are brought into reasonable agreement when expressed in the dimensionless variables  $p = P / \rho_0 c_0^2$ ,  $\eta = \rho / \rho_0$ , and  $e = E / c_0^2$ .

For fixed initial geometry, say that of a sphere or cylinder on a thick plate, the problem parameters for a like-material impact are therefore the material properties  $\rho_0$ ,  $c_0$ , the impact velocity,  $v_0$ , and a characteristic length, such as the projectile diameter,  $L_0$ . From dimensional considerations the solution must be expressible in the form

$$\rho = \rho_0 f_1 \left( \frac{r}{L_0}, \frac{z}{L_0}, \frac{tv_0}{L_0}, \frac{v_0}{c_0} \right),$$

$$P = \rho_0 v_0^2 f_2 \left( \frac{r}{L_0}, \frac{z}{L_0}, \frac{tv_0}{L_0}, \frac{v_0}{c_0} \right),$$

$$u = v_0 f_3 \left( \frac{r}{L_0}, \frac{z}{L_0}, \frac{tv_0}{L_0}, \frac{v_0}{c_0} \right),$$

$$v = v_0 f_4 \left( \frac{r}{L_0}, \frac{z}{L_0}, \frac{tv_0}{L_0}, \frac{v_0}{c_0} \right).$$

The additional assumption that two impacts be late-stage equivalent on the basis of equal  $L_0 v_0^\alpha$ , rather than depending individually on the parameters  $L_0$ ,  $v_0$ , further restricts the form of the solution. It can be shown that under this assumption, the solution must be expressible as

$$\rho = \rho_0 g_1 \left( \frac{R^{\alpha+1}}{\tau^\alpha}, \frac{Z^{\alpha+1}}{\tau^\alpha}, \frac{(v_0/c_0)^\alpha}{\tau} \right),$$

$$P = \rho_0 u_0^2 Z^{-2/\alpha} g_2 \left( \frac{R^{\alpha+1}}{\tau^\alpha}, \frac{Z^{\alpha+1}}{\tau^\alpha}, \frac{(v_0/c_0)^\alpha}{\tau} \right),$$

$$u = v_0 Z^{-1/\alpha} g_3 \left( \frac{R^{\alpha+1}}{\tau^\alpha}, \frac{Z^{\alpha+1}}{\tau^\alpha}, \frac{(v_0/c_0)^\alpha}{\tau} \right),$$

$$v = v_0 Z^{-1/\alpha} g_4 \left( \frac{R^{\alpha+1}}{\tau^\alpha}, \frac{Z^{\alpha+1}}{\tau^\alpha}, \frac{(v_0/c_0)^\alpha}{\tau} \right),$$

where  $\tau = tu_0/L_0$ ,  $R = r/L_0$ ,  $Z = z/L_0$ .

From the first form of the solution, one can conclude, as in Ref. 1, that the solutions for two geometrically similar impacts of the same  $v_0/c_0$  but involving different materials must be the same when expressed in dimensionless variables.

Additional physical conclusions, similar to those obtained for gases, do not appear to be forthcoming. It is not possible, for example, to predict the effects of impact velocity variation from the dimensional analysis results because of the (significant) functional dependence on  $v_0/c_0$ . Further, the late-stage equivalent form of the solution, though simplified, still involves a general functional dependence on three (not two) independent variables. Thus, the property of late-stage equivalence, although verified by the numerical solutions, does not imply a similarity solution in the case of solid-solid impact.

It is apparently necessary to treat numerically a series of impact problems in order to determine the effects of such variations as impact velocity, the shape of the projectile, or the equation of state of the material. To explore these and similar effects, some forty impact interactions have been computed and the results have been analyzed. In the following, the principal conclusions from each study are summarized and results are presented to illustrate specific points.

## 7.2. GENERAL COMMENTS ON A TYPICAL PROBLEM

A typical interaction in the present series is that of a  $10^6$  cm/sec cylindrical lead projectile on a lead target plate, the projectile being 3.6 cm long by 1.8 cm radius. The continuous Eulerian code was used and space resolution was initially defined by square cells 0.1 cm on a side. Each time the disturbance reached the top or right side of the 4300-cell grid, the cell dimensions were doubled by means of a rezoning procedure and additional target material was included. The problem was run to  $2.15 \times 10^2$   $\mu$ sec, at which time the cell dimensions were 0.8 cm, the axial shock penetration distance was approximately 56 cm, and the shock pressure was 25 kbar.

The overall features of the flow are demonstrated by the plots of the velocity and mass flux (or momentum per unit volume) vector fields shown in Figs. 12a and 12b. The shock front in the metal is seen to rapidly assume an approximately hemispherical shape. The motion behind the shock wave is predominately radial, although there is also a definite tendency for this flow to diverge away from the axis and to curl outward toward the target free surface.

Pressure profiles along the axis of symmetry are plotted for various times in Fig. 13. Pressures, especially those less than 100 kbars or so in a metal, are the least precisely defined quantities in the computation. In particular, oscillations in the pressure profile are apparent behind the shock front at intermediate times, and the front is seen to be quite smeared out at late times, when the pressures are in the 25-to 75-kbar range.

The profiles give a reasonable representation of the overall shock attenuation, however, and are also in very good agreement with the expected plane-wave shock pressures at very early times. In general, the Eulerian results on cell-to-cell variation of intensive variables have proved to be more reasonable and substantially smoother (see Section 4) than those obtained from the previous particle-in-cell calculations and have permitted the detailed comparisons of solutions from different problems. Other plots of pressure profiles and also of velocity and density profiles are presented subsequently.

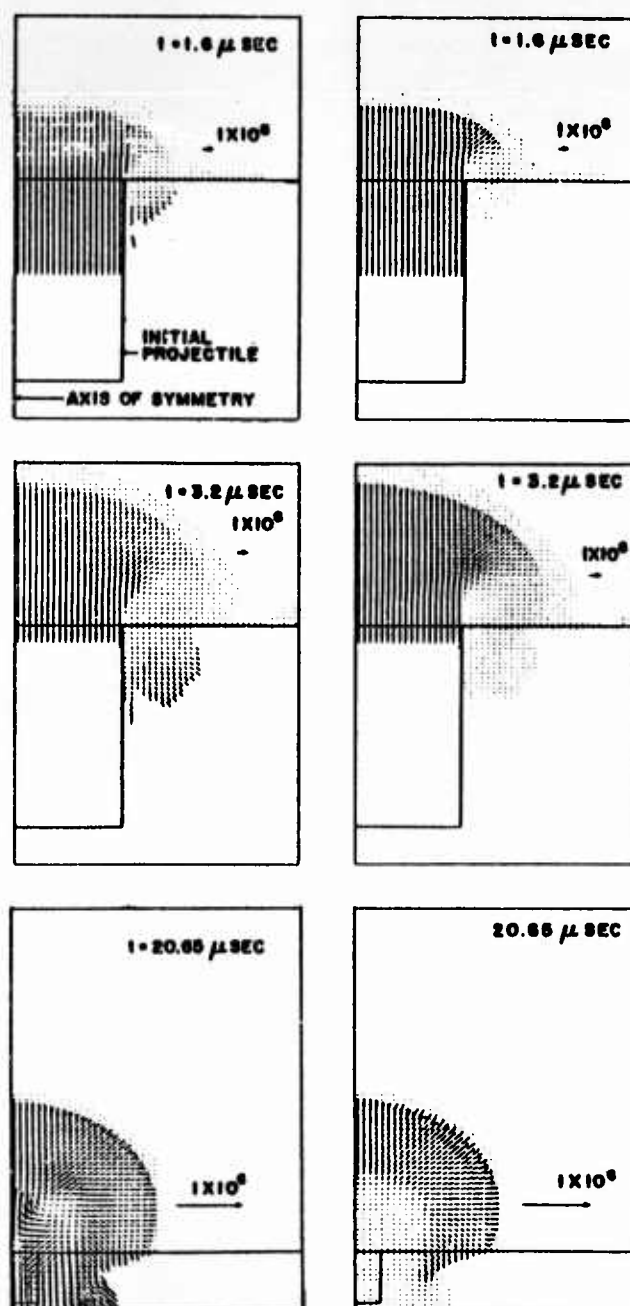


Fig. 12a--Velocity (left) and mass flux (right) vector fields for the  $10^6 \text{ cm/sec}$  lead impact (arrows indicate vector length for  $\vec{u} = 10^6 \text{ cm/sec}$  and  $\rho \vec{u} / \rho_0 = 10^6 \text{ cm/sec}$ )

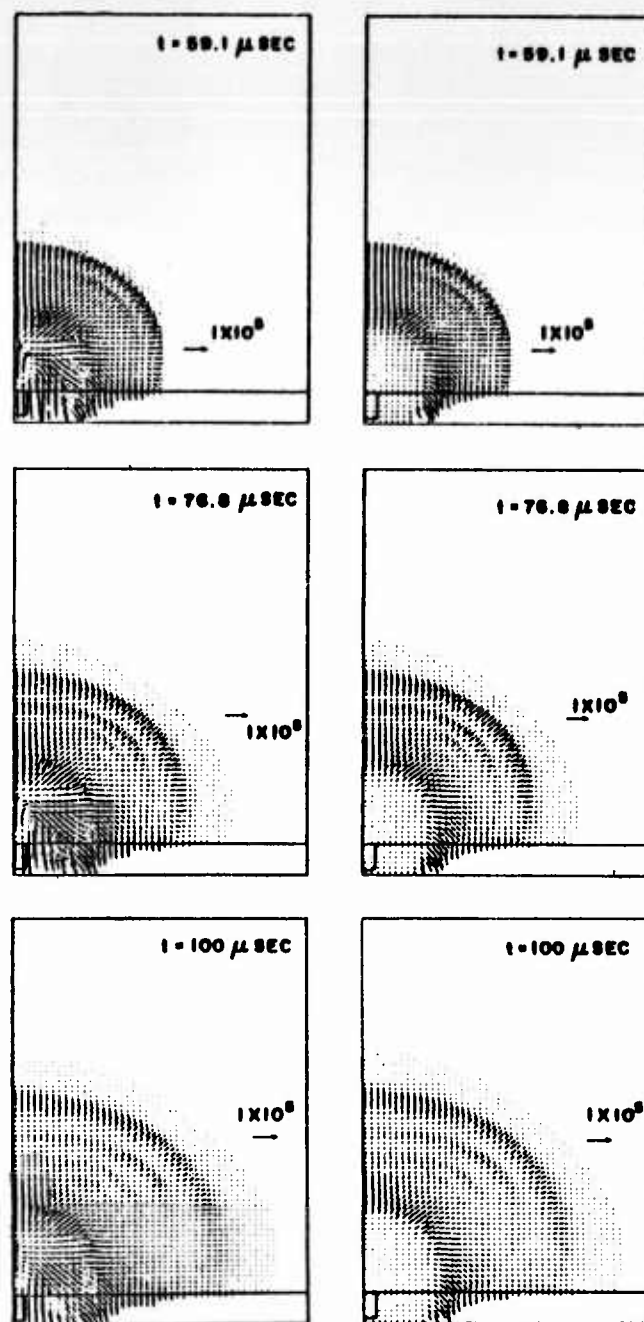


Fig. 12b--Velocity (left) and mass flux (right) vector fields for the  $10^6$  cm/sec lead impact (arrows indicate vector length for  $\vec{v} = 10^5$  cm/sec and  $\rho \vec{u} / \rho_0 = 10^5$  cm/sec)



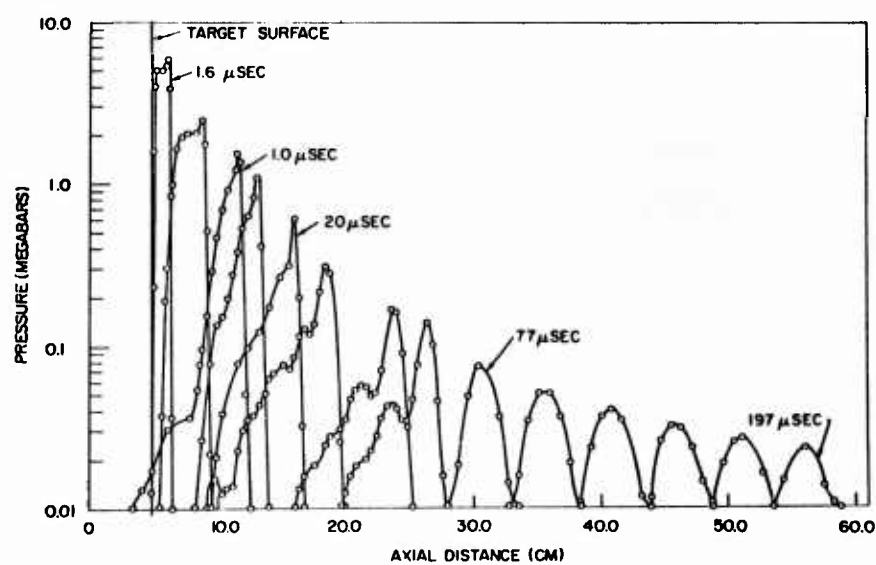
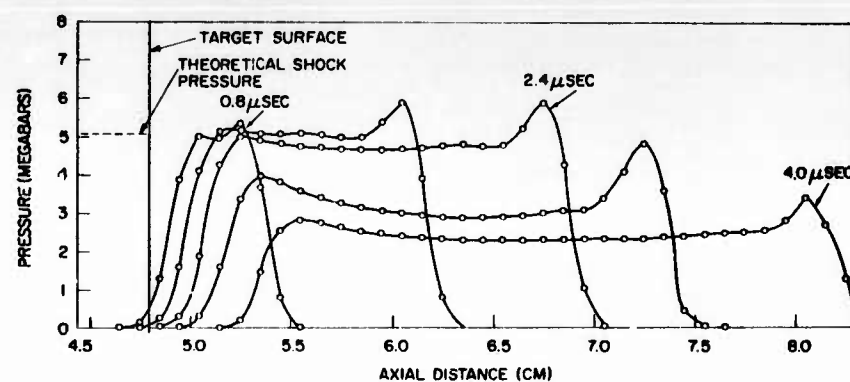


Fig. 13--Axial pressure profiles at various times for the lead-lead impact

Integrated or averaged extensive quantities, such as the total kinetic and internal energies or integrated total momenta, are much more smoothly varying than the intensive cell quantities. Furthermore, changes in mass resolution, space resolution, minor variations in the hydrodynamic code, and variations in the material equation of state have had very small effects on these quantities. For these reasons the integrated variables of the motion, especially of the total momenta, have been used wherever possible for the precise comparison of flows.

### 7.3. VELOCITY LATE-STAGE EQUIVALENCE

A series of like-material impacts has been computed for iron, aluminum, lead, and polyethylene. In each (6-problem) series the impact velocity was varied from  $1.24 c_0$  to  $80 c_0$ , where  $c_0$  is the material "sound speed,"  $c_0 = (\partial P / \partial \rho)_s^{1/2}$ . Thus, the velocities considered range from those attainable experimentally to velocities well in excess of ones of interest in meteoroid impact. The initial geometry for each interaction was that of a right circular cylinder of equal length and diameter interacting with a thick target plate of the same material. Parameters defining the various problems are listed in Table 2.

Table 2  
IMPACT VELOCITIES AND PROBLEM PARAMETERS FOR THE  
SERIES ON CYLINDRICAL PROJECTILE IMPACTS

Series	Iron (cm/sec)	Lead (cm/sec)	Aluminum (cm/sec)	Polyethylene Plastic (cm/sec)	$v_0/c_0$
A	$5 \times 10^5$	$2.5 \times 10^5$	$6.5 \times 10^5$	$3.5 \times 10^5$	1.24
B	$10^6$	$5 \times 10^5$	$1.3 \times 10^6$	$7 \times 10^5$	2.48
A	$2 \times 10^6$	$10^6$	$2.6 \times 10^6$	$1.4 \times 10^6$	4.96
B	$4 \times 10^6$	$2 \times 10^6$	$5.2 \times 10^6$	$2.8 \times 10^6$	9.92
A	$1.6 \times 10^7$	$8 \times 10^6$	$2.1 \times 10^7$	$1.14 \times 10^7$	40
B	$3.2 \times 10^7$	$1.6 \times 10^7$	$4.2 \times 10^7$	$2.28 \times 10^7$	80

Note: For the A series, projectile length and diameter were 3.6 cm and cell dimensions prior to first rezone were 0.1 cm; for the B series, the projectile dimensions were initially 2.4 cm and cell size was the same as in the A series. Exceptions are the first four iron problems, which were somewhat more coarsely zoned.

For each material the problems were planned and analyzed in pairs (1.24 and 2.48  $c_0$ , 4.96 and 9.92  $c_0$ , 40 and 80  $c_0$ ). The purpose was to assure comparable space resolution at late times so that comparison of the two flows for late-stage equivalence could be made without possible bias due to unequal space resolution. In each pair, the twofold increase in impact velocity was offset by reducing the projectile dimensions to  $2/3$  the former values. Thus, the problems were run on a basis intermediate between that given by keeping projectile kinetic energy or projectile momentum constant. More precisely, the indicated change in velocities and dimensions corresponds to  $\alpha = 0.585$ . The close agreement seen below between the as-run problems (prior to changing the relative size of two problems by scaling) therefore corresponds to values of  $\alpha$  which are very near to 0.585.

For the mid- and high-velocity pairs, the detailed comparisons of late stages of the interactions show very good agreement, in both the plots of pressure, density, and velocity profiles from individual cell quantities and in the integrated momentum curves. Typical results of these comparisons are reproduced as Figs. 14, 15, and 16. The very good late-stage agreement of the flows is a gratifying confirmation of the equivalence first reported from the particle-in-cell calculations.<sup>(1)</sup> The present results considerably strengthen the earlier basis for claiming equivalence because the smoother solutions make possible quantitative comparisons of the intensive cell variables, whereas the previous particle-in-cell results necessarily relied primarily on integrated quantities.

For the lowest velocities considered (i.e.,  $5 \times 10^5$  to  $10^6$  cm/sec in iron,  $2.5 \times 10^5$  to  $5 \times 10^5$  cm/sec for lead, etc.), late-stage equivalence is less exact. The radial and axial momentum curves are again brought into good agreement by a single value of  $\alpha$ , but there persists to late times some tendency for the higher velocity impact to be associated with a more intense but narrower pulse. Thus, in the iron pair, the shock for the  $10^6$  cm/sec impact has attenuated to 250 kbar while that for the low-velocity impact is down to 200 kbar at the same radius; for lead, an analogous comparison is 90 and 70 kbar. It seems apparent that the

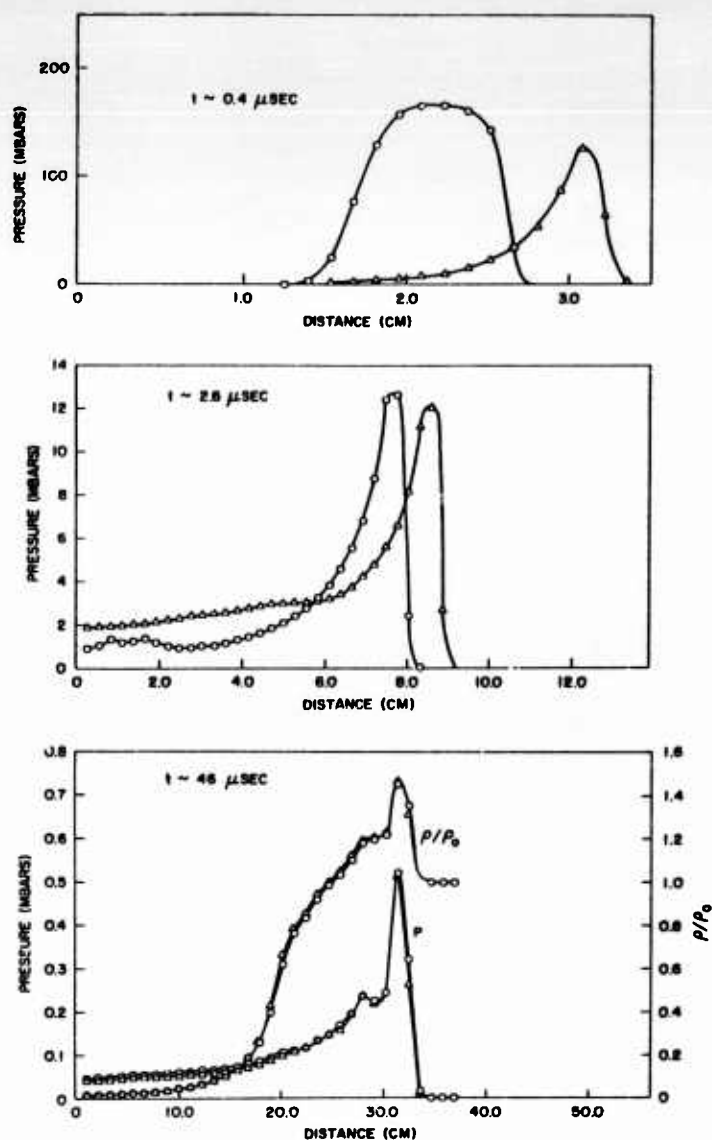


Fig. 14. Convergence to late-stage equivalence of two impact flows. Pressure versus distance at three times and  $\rho/\rho_0$  versus distance at the latest time. Plots are from the  $8 \times 10^6$  cm/sec and  $1.6 \times 10^7$  cm/sec lead impacts. Distance is measured along a line  $45^\circ$  from the axis of symmetry, with origin at the center of impact on the target surface

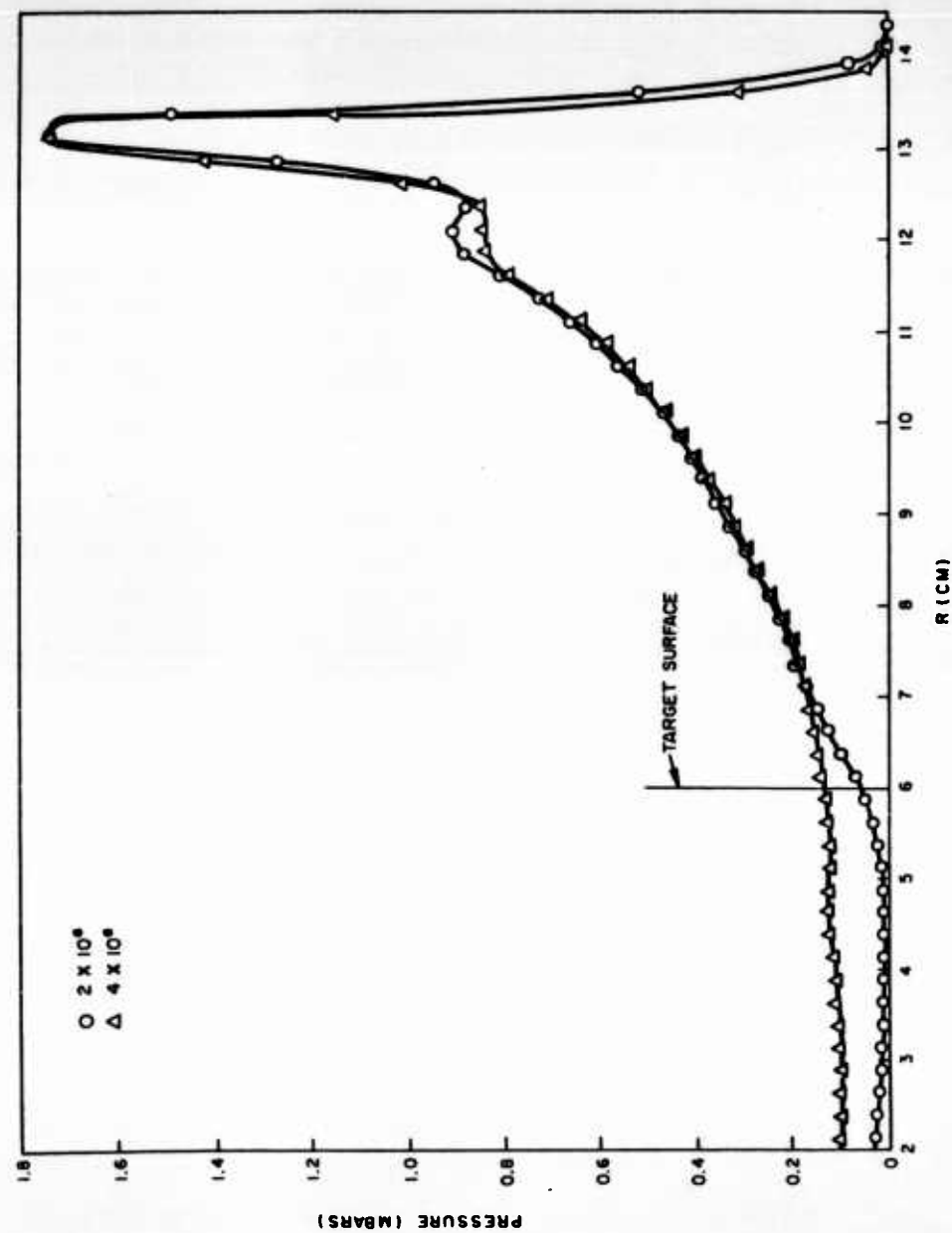


Fig. 15--Comparison of axial pressure profiles for the  $2 \times 10^6$  cm/sec and  $4 \times 10^6$  cm/sec iron impacts, showing late-stage agreement

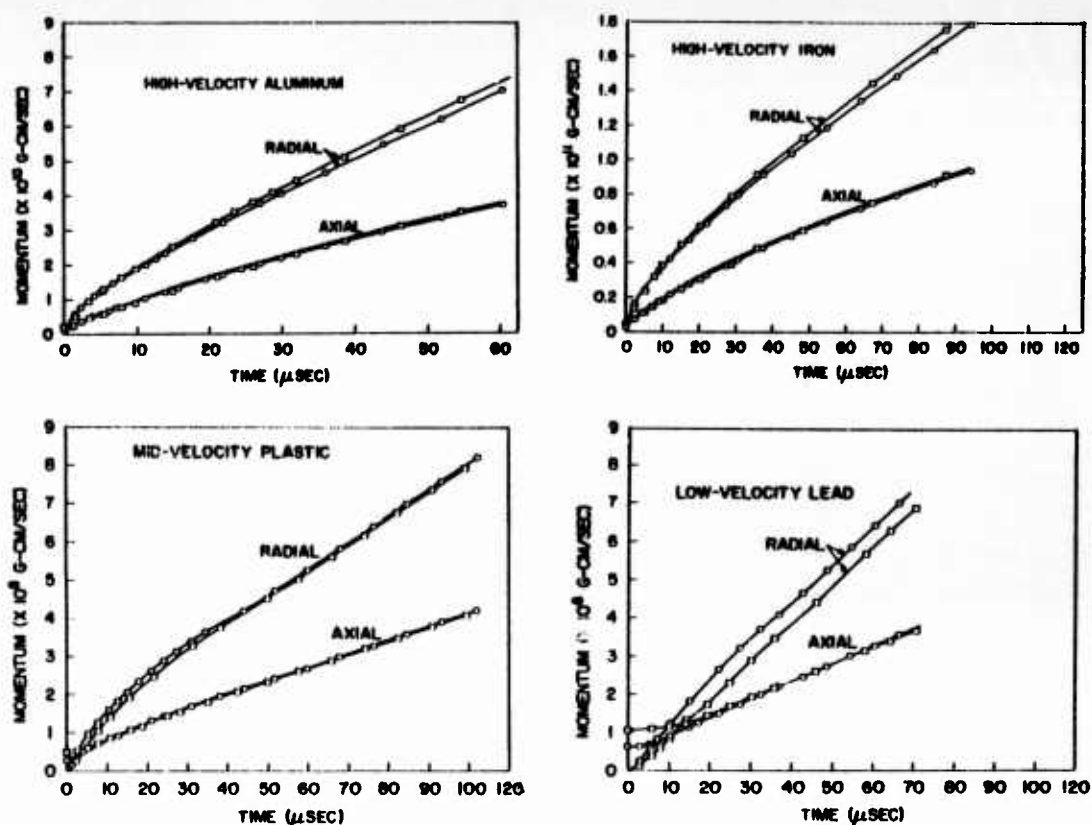


Fig. 16--Comparison of radial and axial momenta; high velocity refers to the two highest velocities given for that material in Table 2, mid velocity refers to the third and fourth highest and low velocity refers to the two lowest velocities; data for the lower-velocity member of each comparison are plotted as circles

failure to achieve precise equivalence is characteristic of low velocities and would become more pronounced if the velocity were further reduced.

Values of  $\alpha$  were obtained from the various comparisons by scaling the relative size of the problems until the best agreement is obtained between the two solutions. (The most precise scale factors are those given by requiring that the axial and radial momenta agree.)  $\alpha$  is then calculated from  $L_1 v_1^\alpha = L_2 v_2^\alpha$ , where  $L_1$  and  $L_2$  are the characteristic linear dimensions after scaling and  $v_1$ ,  $v_2$  are the impact velocities. The results show a remarkable uniformity in  $\alpha$  for all twelve comparisons. Individual values for the eight higher-velocity pairs lie between 0.56 and 0.59 and the low-velocity comparisons indicate values of  $\alpha$  very near 0.60. Precisions on the individual determinations are typically 3% to 4%.

The present results are in substantial agreement with previous values ( $\alpha \cong 0.62$ ) which were obtained for iron from particle-in-cell calculations. The offset of approximately 0.04 is due to a more careful interpretation of the momentum curves, and the present value  $\alpha \cong 0.58$  should be considered more accurate.

#### 7.4. MATERIAL EQUIVALENCE

As was noted previously, the  $\rho_0$ ,  $c_0$  equation-of-state correlation implies that geometrically similar impact problems of equal dimensionless impact velocity,  $v_0/c_0$ , should have the same solution in dimensionless variables. This property of impact hydrodynamics is of some interest because it enables one to generalize computed (or experimental) hydrodynamic results learned from work on only one or two representative materials.

Comparisons to test the proposed equivalence for iron, lead, aluminum and plastic interactions are possible from any pair of problems listed in a given line of Table 2. Dimensionless plots of the momentum curves and representative pressure profiles have been made for each of the possible comparisons and typical results are reproduced as Figs. 17 through 20. The general agreement is seen to be very good. It may be noted that the results for polyethylene correlate somewhat less satisfactorily than those for the metals, as should be expected from the fact that polyethylene was a nonconforming member of the underlying equation-of-state correlation.

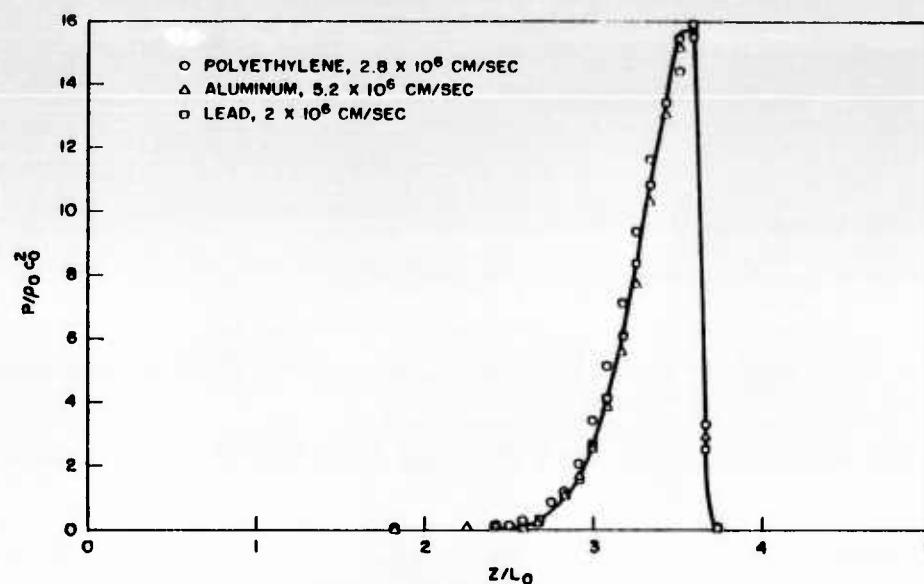


Fig. 17--Comparison of axial pressure profiles in dimensionless variables for polyethylene, aluminum, and lead impacts of equal  $v_0/c_0$

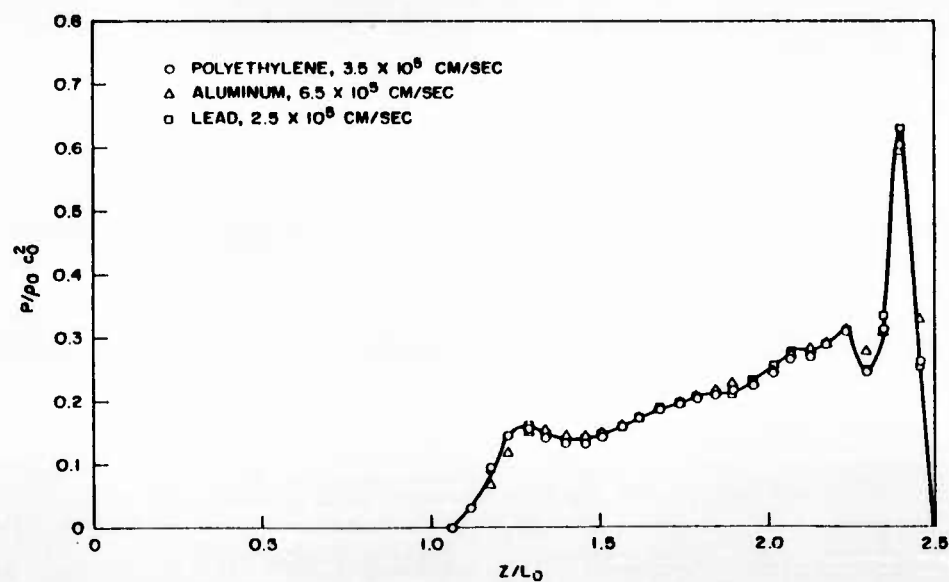


Fig. 18--Comparison of axial pressure profiles in dimensionless variables for polyethylene, aluminum, and lead impacts of equal  $v_0/c_0$



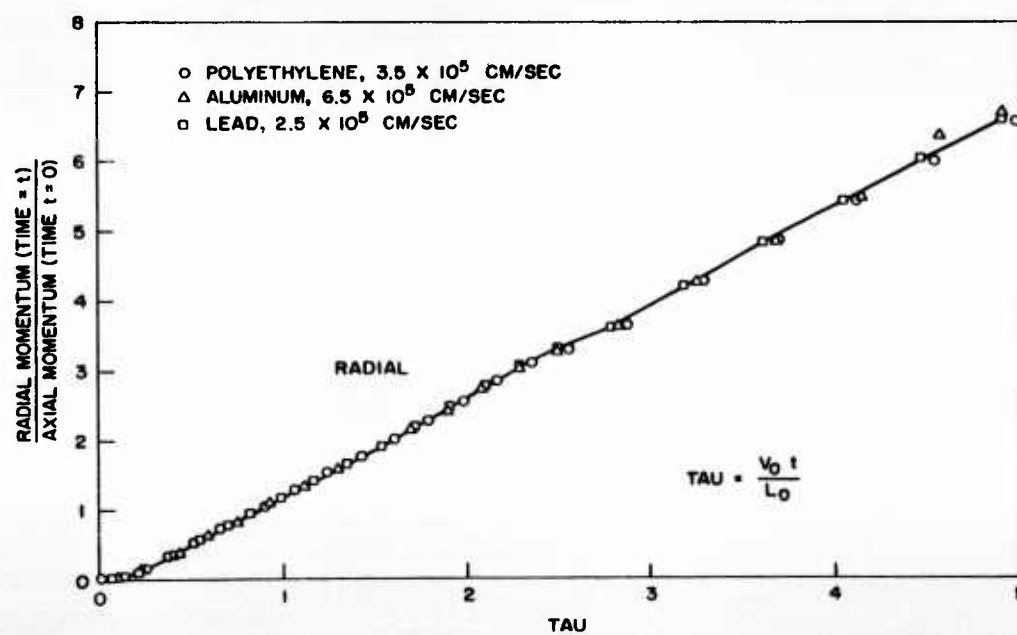
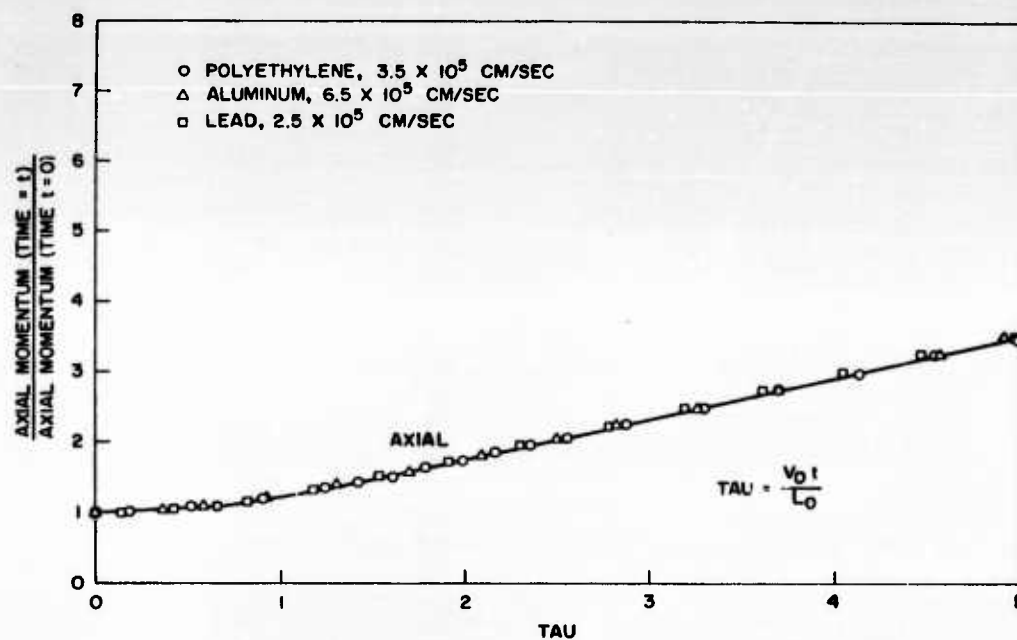


Fig. 19--Comparison of momenta versus time in dimensionless variables for polyethylene, aluminum, and lead impacts of equal  $v_0/c_0$

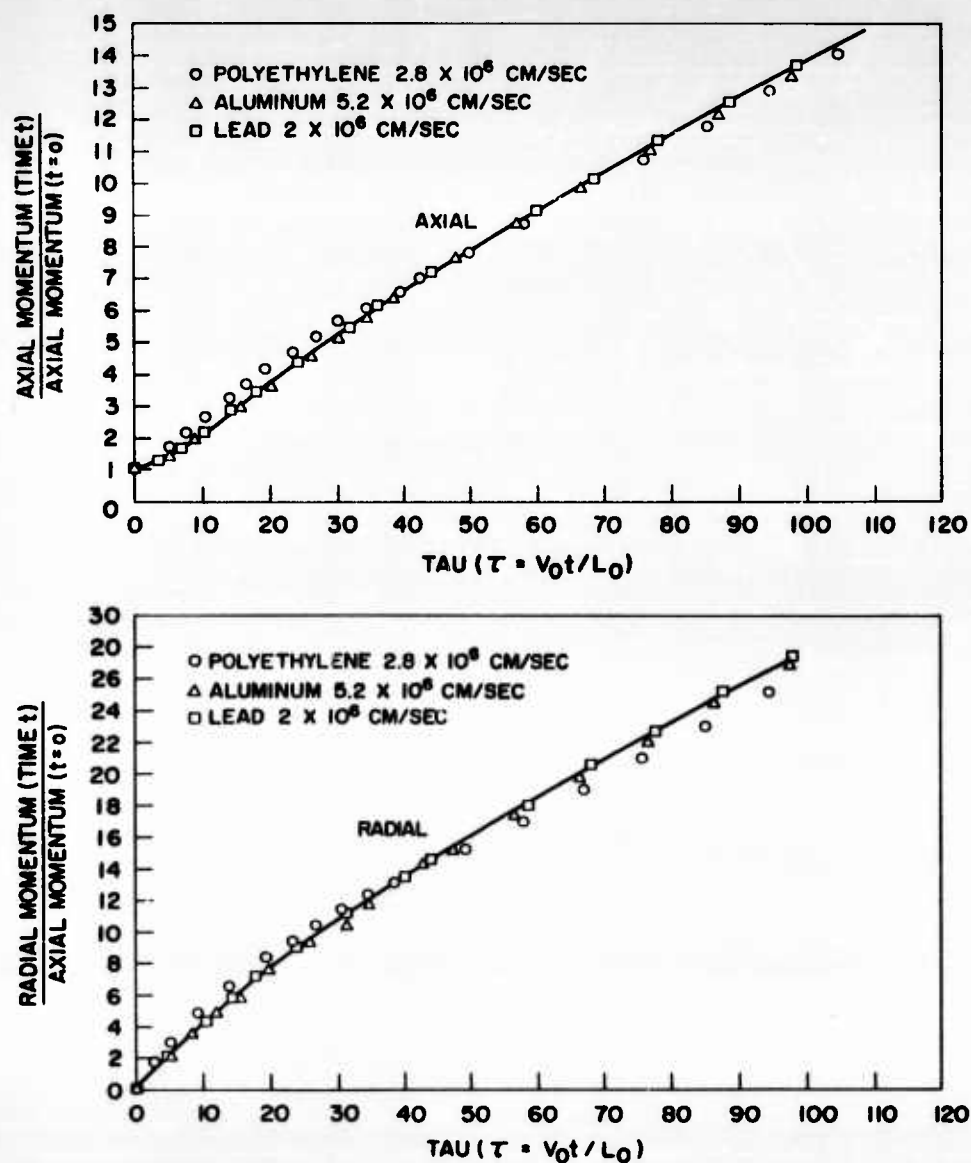


Fig. 20--Comparison of momenta versus time in dimensionless variables for polyethylene, aluminum, and lead impacts of equal  $v_0/c_0$

Additional tests of material equivalence scaling, based on results from particle-in-cell calculations, are described in Ref. 1. The comparisons given there are limited to integrated or averaged quantities but are in good accord with the conclusions given here. The above-reported agreement in the values of  $\alpha$  for the various materials is also to be expected from the equation-of-state correlation.

#### 7.5. PROJECTILE-SHAPE EFFECTS

A series of twelve impact interactions were studied in order to explore effects of projectile shape. Four shapes were considered for each of three impact velocities:

1. Right circular cylinder, equal length and diameter,
2. Sphere,
3. Rod, three diameters long,
4. Disc, three thicknesses in width.

The velocities were  $1.24 c_0$ ,  $4.96 c_0$ , and  $40 c_0$  (corresponding to three of the cylindrical projectile impacts listed in Table 2) and the projectile masses were the same in all problems. The impacting materials were taken to be lead, although the results apply also to other solids by virtue of the material equivalence studies.

In the analysis of the computed results, particular attention was given to determining whether the different projectile shapes lead to a late-stage equivalence and to evaluating the relative effectiveness of the various shapes.

The simplest and most definitive results were obtained in the comparisons of spherical and cylindrical (shape 1, above) projectiles. For each of the three impact velocities, these projectiles lead to practically identical late-stage flows, both in the total axial and radial momenta and in the comparison of instantaneous pressure, density, and velocity plots. Substantial differences are limited to the very early times in which the projectile is embedding itself in the target plate. Finally, the relative scale of the two flows is such that the projectiles are equivalent on an equal-mass basis.

The equivalence of spheres and cylinders has been of some concern in previous investigations, with opinion being divided between equivalence

on the basis of equal projectile mass and the substantially different conclusion that a sphere of given diameter is equivalent to a unit aspect ratio cylinder of that same diameter. Theoretical or computational work on the problem has not been previously reported, however, and the present result is apparently in accord with more recent experimental findings.

Late-stage equivalence is somewhat less exact for the disc and rod projectile geometries. At the two higher velocities, however, the flows are in reasonably good general agreement after a shock penetration distance which is large compared to initial projectile dimensions. This is demonstrated by the vector field plots for the  $4.96 c_0$  ( $10^6$  cm/sec for lead) impact, as seen in Figs. 21 and 22. A close comparison of these results, however, shows that even at late times the disturbance for the rod impact is slightly more elongated in the axial direction than that for either the disc or the sphere. Except for this characteristic of the rod impacts, the late-stage agreement found in the high-velocity comparisons ( $10^6$  and  $8 \times 10^6$  cm/sec) is quite good. Precise comparisons of the momentum curves and the associated scale factors show that the rod impact is equivalent to that for the sphere or cylinder on an projectile equal mass basis. The disc is slightly, but perceptibly, less effective. At both velocities, it would require an increase of some 15% in disc mass for this projectile to be as effective as the others.

The above rod and disc projectiles were purposely chosen to have moderate aspect ratios, with the objective of testing the limits of a late-stage equivalence to show independence of projectile shape. Substantially more extreme aspect ratios will certainly lead to flows which remain qualitatively different throughout the hydrodynamic regime. Such dissimilar flows are, in fact, also evident for the present aspect ratios at the lowest velocity ( $2.5 \times 10^5$ ) studied. The target-plate disturbance due to the rod, for example, was much more concentrated near the axis than that for the disc, and the impact configurations are expected to remain dissimilar indefinitely.

Analytical results can be cited for the limiting extremes of thin-disc and long-rod geometries. For disc projectiles of sufficiently extreme aspect ratio, impact disturbances will become equivalent as essentially plane waves. The slab impact considerations for an ideal gas of  $\gamma = 1.5$ ,

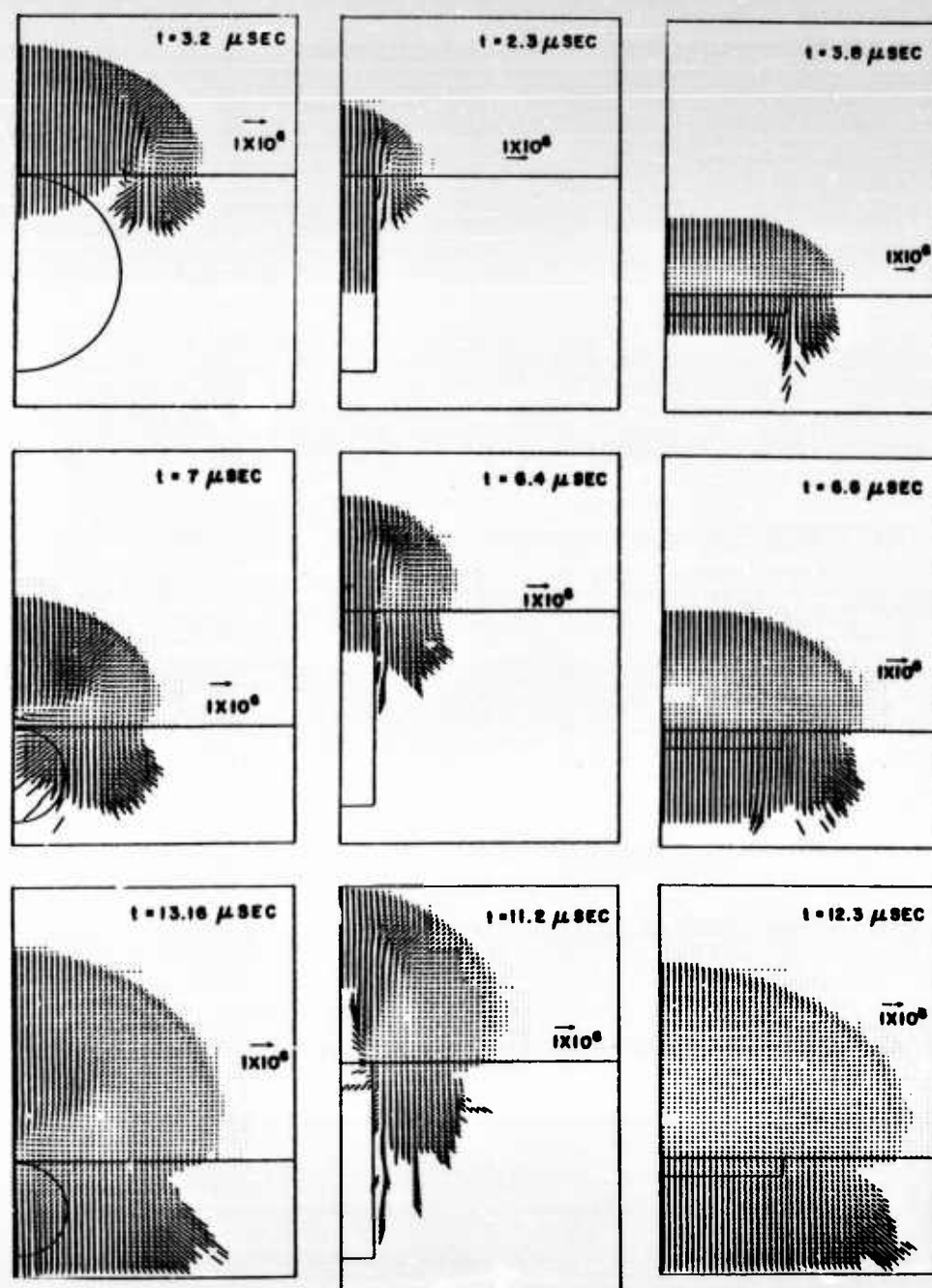


Fig. 21--Velocity fields for the  $10^6$  cm/sec sphere, rod, and disc impacts

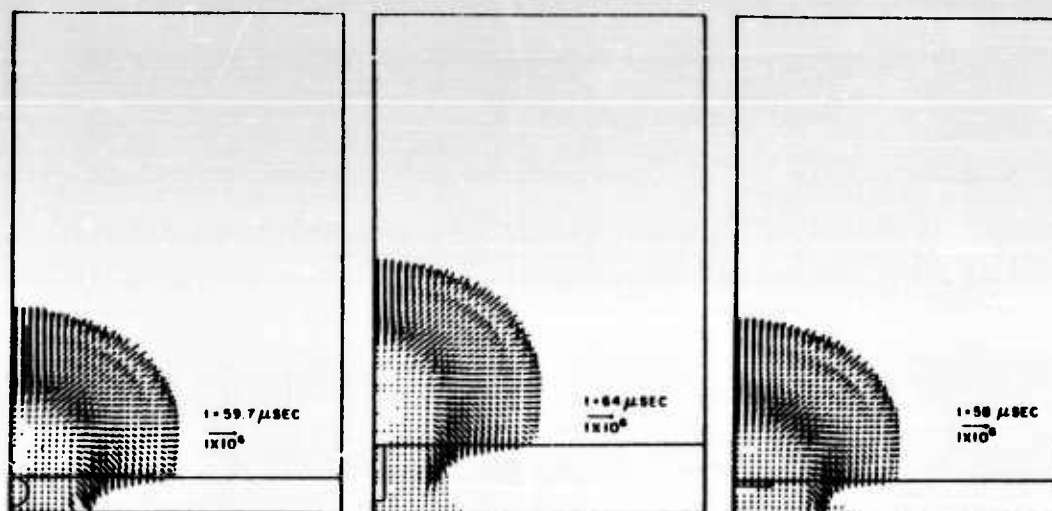


Fig. 22--Comparison of the mass flux on momentum distributions for the sphere, rod, and disc impacts

in particular, indicates equivalence on a basis which is approximately midway between that for equal-energy and equal-momentum projectiles. Because of equation-of-state similarities, the result should apply also to solid impact for sufficiently high velocities and sufficiently extreme disc aspect ratio. It may be that the relative ineffectiveness of the aspect ratio three disc problems is indicative of the fact that  $\alpha$  should decrease to about 0.51 in this limit.

The classical jet-penetration theory applicable to long rod geometries is sufficiently well known that review here is unnecessary. It may be noted, however, that recent applications<sup>(10)</sup> of a jet-penetration model, by Allison and Vitali of the Ballistic Research Laboratories, have led to an extremely encouraging correlation with experimental shock-wave observations of a  $9 \times 10^5$  cm/sec aluminum jet on a plexiglass target. Such considerations are, indeed, quite applicable to the early stages of the rod impacts discussed above.

#### 7.6. DENSITY-EFFECT STUDIES

In most applications, the projectile and target are different materials, and it is desirable to extend present considerations to include such cases.

Dimensional considerations suggest that one should introduce two new parameters to characterize unlike-material impacts--namely, the density and sound speed of the projectile in addition to those of the target. It seems reasonable to assume, however, that variations in projectile density are more significant than those of sound speed, and the subject of unlike-material impact is usually equated to that of density-effect studies.

Several comparisons have been made to evaluate possible effects due to changing projectile density. These include:

1. Three ideal-gas impacts,  $\gamma = 1.5$ , were computed in which the initial projectile density was  $(1.5)^3 = 3.375$  times the target plate density, equal to the target density, and  $(1.5)^{-3}$  times the target density; the initial masses of the three projectiles were the same. The problems were run using the continuous Eulerian code. The calculations were carried to a time about 125-fold greater than the time required for the pellet to bury itself in the target, and detailed cross comparisons of the flows were made in order to evaluate late-stage equivalence and the relative effectiveness of the three densities. When consideration is given to the fact that the total variation in projectile density is by a factor of 11.4, the flows are in remarkably good agreement. Shock penetration distances at late times agree to 10%, with the maximum discrepancy occurring on the axis of symmetry. Axial momenta in the three cases agree within 5%, and the spread in radial momentum is 20% at late times. The direction of indicated discrepancies is such that the high-density projectile is a more effective projectile, but the effect is a negligibly small one.

2. Two calculations were made using special equations of state in order to investigate possible projectile density effects for metal-metal impacts at velocities around  $10^6$  cm/sec. The target material was normal lead and the projectiles were taken to have a modified lead equation of state for which the densities were respectively  $(1.5)^3$  and  $(1.5)^{-3}$  times those of normal lead. This procedure was used to provide a comparison in which the only equation-of-state variation was the density ratio for the target and projectile. The calculations were carried out using the particle-in-cell code, and a relatively high mass resolution of 36 particles per cell was used in order to facilitate the comparison of cell quantities. The two problems were run with equal initial projectile masses. The remarks



made above for gas impacts apply almost verbatim to the present comparison. Axial momenta agree well and the total spread in radial momentum at late times is only 24%. The effects of the 11.4-fold variation in projectile density, with projectile mass kept constant, are quite small; within 20% in projectile mass, the two projectiles are equivalent on an equal-mass basis.

3. Three impacts were computed in which tungsten, iron, and beryllium projectiles interacted with iron targets at a velocity of  $4 \times 10^6$  cm/sec. The particle-in-cell code was used; the interactions were again found to be approximately equivalent at late times for equal initial projectile masses.

Substantial premiums on projectile density have occasionally been reported from empirical correlations<sup>(11, 12)</sup> of experimental impact data. The problem has not been the subject of previous theoretical treatment, however, and the present results are believed to be sufficient to show that such effects do not persist to velocities of  $10^6$  cm/sec and greater.



## 8. OVERALL EFFECTS OF SOLID-SOLID IMPACT

### 8.1. PENETRATION RELATION

The close agreement of two impact flows during the hydrodynamic phase of the interaction is useful when one observes that the subsequent strength-dependent phase of the interaction will also be the same. It follows that the craters in the two cases must agree in shape and in size. This result and the equivalence observations reported in Section 7 can be summarized by the penetration relation

$$p/d = K \left( \frac{\rho_p}{\rho_t} \right)^{1/3} \left( \frac{v}{c_t} \right)^{0.58}.$$

Here  $p$  is the crater depth or some other characteristic crater dimension,  $d$  is the diameter of the projectile if the mass were considered to be a sphere,  $\rho_t$  and  $c_t$  are target density and sound speed,  $\rho_p$  and  $v$  are projectile density and velocity, and  $K$  is a constant to be determined from a single impact experiment. The quantity  $K$  is a constant of the target material, depending on its strength.

From the results given in Section 7, one can expect the penetration relation to be reliable for solid impacts in which (1) the impact velocity is greater than 1–2 times target sound speed; (2) the projectile aspect ratio is within a factor of 3 of unity; and (3) the projectile density is within a factor of about 3 of the target density, which may be too conservative, but additional calculations would be required to confirm this.

### 8.2. MOMENTUM MULTIPLICATION

Another interesting overall effect of a hypervelocity impact is that the momentum transmitted to the target may be many times the momentum of the incident projectile. The dependence of this momentum upon impact velocity is easily determined by recalling from Section 7 that the late-stage momentum depends only on  $M_0 v_0^{3\alpha}$  rather than on  $M_0$ ,  $v_0$  individually.

That is,

$$I = f(M_0 v_0^{3\alpha}).$$

On the other hand, simple linear scaling shows that impulse must be directly proportional to projectile mass  $M_0$ , so that this functional dependence must be

$$I = k M_0 v_0^{3\alpha}.$$

where  $k$  is a constant. Finally, momentum multiplication, defined as the ratio of total target impulse to initial projectile momentum, satisfies

$$M_m = \frac{k M_0 v_0^{3\alpha}}{M_0 v_0} = k v_0^{3\alpha - 1}.$$

Hence, momentum multiplication increases as the 0.74 power of impact velocity, when the value  $\alpha = 0.58$  is taken into account.

### 8.3. TARGET-HARDNESS EFFECTS

There has been some interest in the past as to whether target hardness (known to play an important role in limiting crater size at low impact velocities) persists in dominating crater size as the velocity is increased. The affirmative answer to this question leads to the conclusion that a reasonable estimate of crater size cannot be made using theoretical hydrodynamic results only.

An important experimental study of this question was made recently by J. H. Kineke and L. G. Richards.<sup>(13)</sup> Velocities of  $9.7 \times 10^5$  cm/sec and  $1.55 \times 10^6$  cm/sec were attained for aluminum and beryllium projectiles, respectively, both of which were fired into soft and hard aluminum targets. The ratio of crater volumes in the two targets (same impacting projectile) was found to be a constant, about 3, for the entire range of impact velocities from a few times  $10^5$  cm/sec to the maximum values given above. Thus, target-strength effects continue to influence crater dimensions up to the highest impact velocities attained.

The Kineke-Richards result is precisely the one which should be expected from late-stage equivalence. Consider, for example, a pair of

impacts (hard and soft targets) at  $5 \times 10^5$  cm/sec. The pair will obviously be identical in the hydrodynamic phase, because the hydrodynamic equations of state are the same. This pair is also late-stage equivalent to another pair (hard and soft targets) at  $1.5 \times 10^6$  cm/sec. Hence, all four impacts lead to the same late-stage deformation problem. A ratio of 3 in crater volumes for the low-velocity pair, in particular, must also apply to the  $1.5 \times 10^6$  cm/sec experiments. Target-strength effects do not become less important as impact velocity is increased.

## 9. CONCLUDING REMARKS

### 9.1. PRINCIPAL CONCLUSIONS

The principal conclusions from the present work are that

1. Crater dimensions increase as the 0.58 power of the impact velocity.
2. Changing projectile density at constant projectile mass leaves unchanged the overall effects on the target.
3. Spherical and unit-aspect-ratio cylindrical projectiles of equal mass have equivalent impact effects except at very early times. Projectile aspect ratios as extreme as 3 are unimportant for impacts at five times target sound speed and greater.
4. Target strength plays an important role in limiting crater size even for arbitrarily high velocities. The ratio of crater dimensions for hard and soft targets is independent of the impact velocity.
5. The ratio of total target impulse to initial projectile momentum increases as the 0.74 power of the impact velocity.

Conclusions (1), (4), and (5) are applicable to impact velocities which are greater than about twice target sound speed, and (2) pertains to impact velocities greater than about five times target sound speed.

Conclusion (1) is in good general agreement with the 0.62 power dependence reported previously.<sup>(1)</sup> The basis for this result has, however, been considerably strengthened in the present investigation: The hydrodynamic calculations have been extended to much later times and to pressures (0.1 Mbar and less) which are typically an order of magnitude lower. More important, the smoothness of the continuous Eulerian solutions permits one to make detailed comparisons of plots of the intensive variables made from listings of individual cell quantities. Such comparisons (e.g., Fig. 14) confirm the earlier claim that flows at different impact velocities are late-stage equivalent.

## 9.2. EXPERIMENTAL-THEORETICAL CORRELATIONS

Results of the present investigation appear to be in good agreement with the main body of experimental data. The results of comparisons with recent experimental findings are briefly summarized below:

1. Penetration Exponents. The value  $2/3$  for  $\alpha$  has frequently been quoted from summaries<sup>(11, 14)</sup> of available experimental knowledge. Energy equivalence ( $\alpha = 2/3$ ) was also reported by Kineke and Richards<sup>(13)</sup> from aluminum data extending to  $9.7 \times 10^5$  cm/sec. Also Halperson's recent 1100F data for aluminum,<sup>(15)</sup> extending to  $7 \times 10^5$  cm/sec, appear to us to be quite reasonably fitted by a constant exponent  $\alpha = 1/2$ .

The present theoretical result for aluminum is that  $\alpha = 0.58$  for velocities above about  $10^6$  cm/sec. The agreement with experiment seems very satisfactory, especially when account is taken of the fact that the experimental values must be obtained by differentiating penetration data and accordingly apply for velocities somewhat less than the upper limit of the data.

2. Momentum Multiplication. Total target impulses that are greater than the initial pellet momentum have been observed experimentally. In a previous progress report (see Ref. 20a) it was shown that recent data<sup>(16)</sup> for lead were compatible with conclusion (5), above.

3. Target Strength. The experimental findings by Kineke and Richards were discussed in Section 8 and seen to be in agreement with the theoretical result on persistence of strength effects at high velocities.

## 9.3. COMPARISON WITH OTHER THEORETICAL RESULTS

The first application of hydrodynamic codes to the impact problem was the well-known work by Bjork.<sup>(17)</sup> Aluminum-aluminum and iron-iron impacts were treated at velocities of  $5.5 \times 10^5$  cm/sec,  $2 \times 10^6$  cm/sec, and  $7.2 \times 10^6$  cm/sec.

While present results and those by Bjork are apparently in reasonable agreement for the so-called hydrodynamic phase, an important difference in the two approaches arises in the methods used to determine the penetration relation. Bjork obtained penetrations by estimating the stage at which

strength effects would arrest the hydrodynamics. From three such estimates for each metal he concluded that penetration increases as the  $1/3$  power of the impact velocity.

In his recent discussion<sup>(18)</sup> for the Sixth Symposium on Hypervelocity Impact, however, Bjork revised his earlier penetrations for impact velocities greater than about  $2 \times 10^6$  cm/sec. The new penetration for velocity  $7.2 \times 10^6$  cm/sec was estimated to be some 40% higher than the old one. The correction, made to take better account of melting, was given as a rough estimate. This estimated correction is quite important, accounting for about one-half the discrepancy between Bjork's old data and our present result.

It seems desirable to await a more complete evaluation of the melting effect before attempting to decide whether a significant difference exists in the two approaches. It is of interest to note, however, that the remaining discrepancy is substantially less than that for the extremes of energy equivalence,  $\alpha = 2/3$ , and momentum equivalence,  $\alpha = 1/3$ . These  $\alpha$ 's, if used to extrapolate the experimental data by a factor of 10, lead to penetrations (suitably chosen scale) of 214 and 100 for  $\alpha = 2/3$  and  $\alpha = 1/3$ , respectively. On this same scale the penetration for  $\alpha = 0.58$  is 174 and Bjork's revised penetration is 140.

It should be remarked, in connection with melting, that the method used in the present effort does not require a knowledge of the effects of melting or of shock heating on target strength. The approach depends on showing merely that two impacts are hydrodynamically equivalent prior to the onset of the strength-dependent deformation phase.

Riney has very recently published some interesting new results.<sup>(19)</sup> A particle-in-cell code was applied to aluminum-aluminum and lead-lead impacts, and the conclusion was reached that impacts are late-stage equivalent on an equal-energy, or  $\alpha = 2/3$ , basis. It was further concluded that target-strength effects do not vanish as impact velocity increases.

The general agreement between Riney's results and the present investigation is very encouraging. Riney does not claim a theoretical basis for exact energy equivalence, however, and none has ever been given. Indeed, our most important general conclusion from the one-dimensional impact, the axisymmetric ideal-gas impact, and the work on solid-solid

impact is that impacts are equivalent on a basis intermediate between equal projectile momentum and equal projectile energy. For the important case of solid-solid impact at velocities in the meteoric range, energy equivalence is more nearly correct.

## REFERENCES

1. Walsh, J. M., and J. H. Tillotson, "Hydrodynamics of Hypervelocity Impact," General Atomic, Report GA-3827, Contract AF29(601)-4759, January, 1963. Also in Proceedings of the Sixth Symposium on Hypervelocity Impact, Vol. II, Part I, August, 1963.
2. Tillotson, J. H., "Metallic Equations of State for Hypervelocity Impact," General Atomic, Report GA-3216, Contract AF29(601)-4759, July, 1962.
3. Evans, M. W., and F. H. Harlow, "The Particle-in-Cell Method for Hydrodynamic Calculations," Los Alamos Scientific Laboratory, Report LA-2139, November, 1957.
4. Harlow, F. H., "Two-Dimensional Hydrodynamic Calculations," Los Alamos Scientific Laboratory, Report LA-2301, September, 1959.
5. Johnson, W. E., "Computer Development to Improve SHELL Code," General Atomic, Report GA-4673, Contract AF29(601)-6028, October, 1963.
6. Courant, R., and K. O. Friedrichs, Supersonic Flow and Shock Waves, Interscience Publishers, Inc., New York, 1948.
7. Nowak, M. J., "A Systematic Study of Some Self-similar Solutions," General Atomic, Report GA-5058, Contract DA-04-495-AMC-116(X) (to be published).
8. Häfele, W., "Zur analytischen Behandlung ebener, starker, instationärer Stosswellen," Z. Naturforsch., Vol. 10a, 1955, p. 1006.
9. Rae, W. J., and H. P. Kirchner, "Final Report on a Study of Meteoroid Impact Phenomena," Cornell Aeronautical Laboratory, Report RM-1655-M-4, February, 1963. Also summarized in Proceedings of the Sixth Symposium on Hypervelocity Impact, Vol. II, Part I, August, 1963.
10. Allison, F. E., and R. Vitali, Ballistic Research Laboratories (unpublished).



11. Hermann, W., and O. F. Jones, "Survey of Hypervelocity Impact Information," Massachusetts Institute of Technology, Report HSRL 99-1, October, 1961.
12. Olshaker, A. E., and R. L. Bjork, "Scaling Laws for Dissimilar Materials," Proceedings of the Fifth Symposium on Hypervelocity Impact, Vol. I, April, 1962, p. 185.
13. Kineke, J. H., and L. G. Richards, "Influence of Target Strength on Hypervelocity Crater Formation in Aluminum," Proceedings of the Sixth Symposium on Hypervelocity Impact, Vol. II, Part 2, August, 1963.
14. Eichelberger, R. J., and J. W. Gehring, "Effects of Meteoroid Impacts on Space Vehicles," Am. Rocket Soc. J., Vol. 32, No. 10, October, 1962, p. 1583.
15. Halperson, S. M., "Some Phenomena Associated with Impacts into Aluminum," Proceedings of the Sixth Symposium on Hypervelocity Impact, Vol. II, Part 2, August, 1963.
16. Becker, K. R., R. W. Watson, and F. C. Gibson, "Hypervelocity Impact Phenomena Quarterly Report," Bureau of Mines, Report AD 278641, May, 1962.
17. Bjork, R. L., "Effects of Meteoroid Impact on Steel and Aluminum in Space," The RAND Corporation, Paper P-1662, December, 1958.
18. Bjork, R. L., "Review of Physical Processes in Hypervelocity Impact Penetration," Proceedings of the Sixth Symposium on Hypervelocity Impact, Vol. II, Part 1, August, 1963.
19. Riney, T. D., "Theoretical Hypervelocity Impact Calculations Using the PICKWICK Code," Space Sciences Laboratory, Missile and Space Division, General Electric, Report R64SD13, February, 1964.
20. Quarterly progress reports under the present contract, General Atomic Reports:
  - (a) GACD-4277 of April, 1963
  - (b) GACD-4518 of July, 1963
  - (c) GACD-4793 of October, 1963Most of the material in these reports is superseded by the present summary report.

**UNCLASSIFIED**

**UNCLASSIFIED**